JM PAPERS

Direct numerical simulation of supersonic boundary layers over a microramp: effect of the Reynolds number

G. Della Posta[1],†, **M. Blandino**[1], **D. Modesti**[2], **F. Salvadore**[3] and **M. Bernardini**[1]

[1]Department of Mechanical and Aerospace Engineering, Sapienza University of Rome, via Eudossiana 18, 00184 Rome, Italy

[2]Aerodynamics Group, Faculty of Aerospace Engineering, Delft University of Technology, Kluyverweg 2, 2629 HS Delft, The Netherlands

[3]HPC Department, CINECA, via dei Tizii 6/B, 00185 Rome, Italy

Microvortex generators are passive control devices smaller than the boundary layer thickness that energise the boundary layer to prevent flow separation with limited induced drag. In this work, we use direct numerical simulations (DNS) to investigate the effect of the Reynolds number in a supersonic turbulent boundary layer over a microramp vortex generator. Three friction Reynolds numbers are considered, up to $Re_\tau = 2000$, for fixed free stream Mach number $M_\infty = 2$ and fixed relative height of the ramp with respect to the boundary layer thickness. The high-fidelity data set sheds light on the instantaneous and highly three-dimensional organisation of both the wake and the shock waves induced by the microramp. The full access to the flow field provided by DNS allows us to develop a qualitative model of the near wake, explaining the internal convolution of the Kelvin–Helmholtz vortices around the low-momentum region behind the ramp. The overall analysis shows that numerical results agree excellently with recent experimental measurements in similar operating conditions and confirms that microramps effectively induce a significantly fuller boundary layer even far downstream of the ramp. Moreover, results highlight significant Reynolds number effects, which in general do not scale with the ramp height. Increasing Reynolds number leads to enhanced coherence of the typical vortical structures in the field, faster and stronger development of the momentum deficit region, increased upwash between the primary vortices from the sides of the ramp – and thus increased lift-up of the wake – and faster transfer of momentum towards the wall.

Key words: boundary layer control, compressible boundary layers, vortex dynamics

† Email address for correspondence: giacomo.dellaposta@uniroma1.it

974 A44-1

1. Introduction

The interaction between shock waves and boundary layers has been widely studied during the last 70 years and is still the subject of extensive research, because of its frequent occurrence in many aerospace systems (Dolling 2001; Gaitonde 2015). Shock wave/boundary layer interactions (SBLIs) can be found in a wide range of flows including transonic airfoils, high-speed inlets, control surfaces of high-speed aircraft, space launchers base flows and overexpanded nozzles. In the interaction region, extreme, unsteady, mechanical and thermal loads are typically observed (Clemens & Narayanaswamy 2014), and the adverse pressure gradient imposed by the shock often causes the boundary layer to separate intermittently (Bernardini *et al.* 2023*a*). This problem represents, for example, a critical issue for high-speed intakes, since the low-momentum separated flow affects the mass flow rate entering the engine, producing flow distortions, total pressure losses and potential inlet unstarts (Herrmann & Koschel 2002).

Given its pivotal importance, it is evident that alleviating the detrimental effects of SBLI by means of control devices would have a significant impact on the performance and the reliability of many aerospace engineering systems (Babinsky & Ogawa 2008). The most widespread solution to delay shock-induced separation in high-speed intakes, and to control SBLI in turn, is the so-called boundary layer bleed, which consists in diverting the separated flow near to the wall out of the engine. Removing low-momentum fluid makes the boundary layer more resistant to shock-induced separation and reduces the distortion of the flow ahead of the engine too. However, since the bled air is not reinjected elsewhere, the flow rate is reduced up to 15 %–20 % (Loth 2000), requiring an increase in the intake frontal area and, in turn, an increase in the aerodynamic drag of the vehicle. Other solutions have thus been explored, like classical vortex generators (VGs) (Davis & Mitchell 1968), especially with vane-type form. Classical VGs, whose heights are larger than the boundary layer thickness, generate passively trailing vortices that bring high-momentum flow from outside the boundary layer to the near-wall region. However, despite their benefits, VGs generate considerable additional drag.

To leverage the same mechanism of VGs and energise the near-wall region of the boundary layer upstream of the interaction, microvortex generators (MVGs) have been proposed (Wheeler 1984; McCormick 1993), with heights smaller than the boundary layer thickness. Compared with their traditional counterpart, MVGs offer the same control efficiency but with a decreased wave drag, given their reduced height (Lin 2002). Among the various configurations proposed, although microvanes seem to be slightly more effective, microramps are typically preferred because of their superior mechanical robustness. In fact, MVGs are usually mounted upstream of the SBLI, and thus, in case of failure, their ingestion would bring catastrophic consequences for the inlet.

During the last twenty years, research has focused particularly on the characterisation of the wake downstream of microramps and on its influence on SBLI separation (Lu, Li & Liu 2012; Panaras & Lu 2015). As a matter of fact, the control mechanism of microramps relies on how these change the flow topology upstream of the interaction. Therefore, a deep understanding of the complex structure of the wake produced by a microramp in a high-speed boundary layer is essential and preliminary to the assessment of any effect MVGs may have on SBLI. The first extensive description of the mean flow behind an MVG was due to Pitt Ford & Babinsky (2007) and Babinsky, Li & Ford (2009). The authors analysed through surface oil visualisations the different large-scale structures emerging from the interaction between a microramp and a supersonic boundary layer. Firstly, the incoming flow is subjected to compression on the microramp leading edge, which leads to
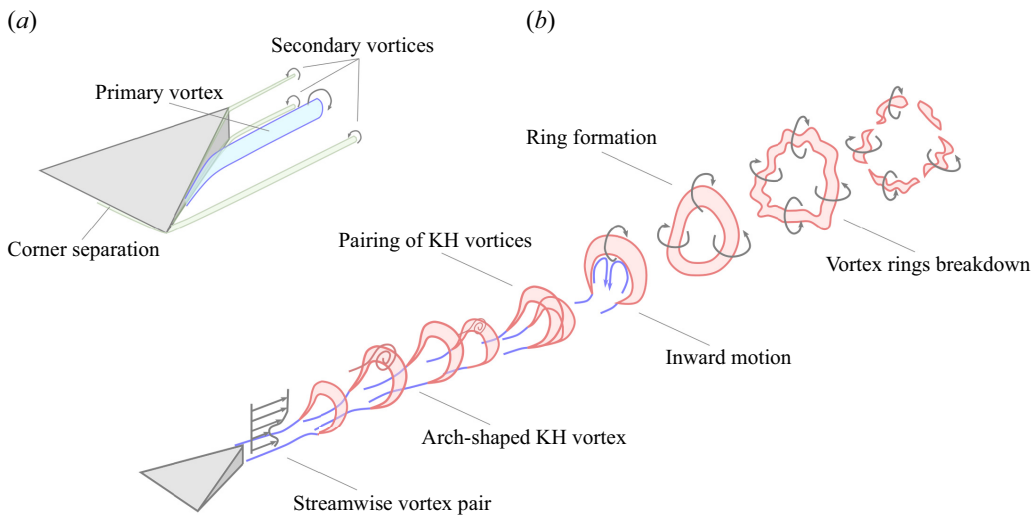
Figure 1. Mean vortical structures in the model of Babinsky *et al.* (2009) (*a*) and instantaneous flow organisation according to the model of Sun *et al.* (2014*b*) (*b*).

a small pocket of separated flow and to the development of a horseshoe vortex. Then, the fluid flows on top of the ramp, turning laterally towards the ramp edges, where it separates from the device and generates a pair of counter-rotating vortices on the two ramp sides, the so-called primary vortex pair. The vortex pair brings high-momentum flow from the outer region of the boundary layer down towards the wall, inducing a fuller boundary layer which is less prone to separation. In addition to these primary structures, a series of secondary vortices also originates from the bottom and top edges of the device (Lu *et al.* 2010). Downstream of the microramp trailing edge, the two primary vortices become parallel and autoinduce a vertical force in the plane of symmetry that causes the wake and the vortex pair to lift up. Therefore, moving downstream, the wake lift-up, together with viscous and turbulent dissipation, progressively weaken the energising mechanism of the wake, which eventually returns to the undisturbed conditions. A qualitative representation of the mean vortex structure behind the microramp is reported in figure 1(*a*).

Other studies have instead investigated the instantaneous organisation of the flow field behind the microramp. Blinde *et al.* (2009) analysed the effect of an array of microramps on a boundary layer at $M_\infty = 1.84$ through stereoscopic particle image velocimetry (PIV), where $M_\infty = U_\infty/c_\infty$ is the Mach number based on free stream velocity and the speed of sound. From the distribution of the velocity on two planes parallel to the wall, the authors inferred the presence of a train of hairpin vortices surrounding the primary streamwise vortices. Implicit large eddy simulations (ILESs) of a microramp in a turbulent boundary layer at $M_\infty = 2.5$ by Li & Liu (2011) revealed instead the existence of a train of ring-shaped vortices surrounding the low-momentum region that induces significant wake meandering. According to the authors, these large-scale structures are generated by a Kelvin–Helmholtz (KH) instability originating from the shear layer that envelops the momentum deficit in the microramp wake. In their experimental analysis of a boundary layer at $M_\infty = 2.7$, Bo *et al.* (2012) observed that these KH vortices are characterised by a frequency between 50 and 60 kHz, which is transferred to the reflected shock downstream, as the intermittent structures pass through the interaction zone and deform the shock system. Vortex rings from microramps pass across the SBLI without losing their coherence and disrupt the separation bubble according to their shedding frequency, which thus makes

them a key component in the control mechanism of SBLI (Grébert *et al.* 2018). To better understand the evolution of the wake behind microramps and to solve the controversy in the different vortex models proposed by many authors, an extensive investigation on the flow generated by a microramp in a turbulent boundary layer at $M_\infty = 2.0$ was carried out through tomographic PIV and ILES in Sun *et al.* (2012, 2013, 2014*b*). Based on the previous findings and on their results, the authors proposed a conceptual model (see figure 1*b*) in which arc-shaped KH vortices surrounding the primary vortex pair develop at first, right behind the ramp. As the lift-up induced by the primary vortex pair acts on the wake, the arc legs are subjected to an inward movement that leads to the formation of closed vortex rings. These periodic entities then modulate the primary vortex pair and finally undergo turbulent distortion that eventually breaks them down.

Even if comprehensive experimental studies like the ones presented above are paramount, their inherent restrictions in terms of spatial accuracy and data accessibility limit their ability to fully understand how MVGs may control SBLI. For instance, in many studies, flow features are observed only on a limited number of planes, like the vertical symmetry plane. However, the field is highly three-dimensional (3-D), and the interpretation of the measurements on these surfaces may be misleading with respect to the global flow structure. High-fidelity numerical simulations thus represent a valid complementary tool that has proved effective in overcoming such limitations. As a result, detailed numerical data may help address the physical questions remaining in some way open, like the effect of the Mach and Reynolds numbers on the strength and decay of the time-averaged and instantaneous wake features or the precise role that KH instability has in the control mechanism of SBLI.

To the authors' knowledge, a limited number of numerical studies have been carried out to fully comprehend the flow alteration induced by a microramp, and mainly using Reynolds-averaged Navier–Stokes simulations (RANSs) (Ghosh, Choi & Edwards 2010) or ILESs (Lee & Loth 2009; Li & Liu 2010, 2011; Lee *et al.* 2011; Sun *et al.* 2014*a*), with momentum thickness-based Reynolds numbers $Re_\theta \in [1400, 5800]$. Both numerical techniques rely on closure assumptions, which can lead to model-dependent results, especially in the case of RANS of separated flows. Despite the higher uncertainty of RANS, however, this tool remains the only possibility to explore a large parameter space. For example, Anderson, Tinapple & Surber (2006) carried out a multiobjective optimisation of the microramp geometry using RANS, with the aim of minimising the total pressure loss across the SBLI and the boundary layer shape factor H. The result has been deliberately taken as the baseline, optimal case by the majority of the cited studies.

Although similar methodologies allowed researchers to better describe the evolution of the main vortical structures and to refine models based on experiments, they are not fully able to capture the unsteady and multiscale nature of the flow under consideration. However, thanks to the technological developments in high-performance computing (HPC) and to the advent of the graphics processing unit (GPU) technology for scientific simulations, we are today able to perform direct numerical simulations (DNSs) with parameters that are comparable with those of real experiments. By solving Navier–Stokes equations directly, without relying on any modelling assumption, such simulations are able to produce results with the highest level of detail possible, which is crucial to improve our physical grasp of complex flow cases like the one considered in this work. Additionally, high-fidelity numerical simulations provide accurate and comprehensive data that can help better calibrate lower-fidelity or reduced-order models, to conduct, for example, optimisation studies for practical applications.

For this reason, we present here the results of a set of DNSs of a supersonic turbulent boundary layer over a microramp.

The geometry considered is the one of the optimal microramp defined by Anderson *et al.* (2006), and the free stream Mach number is equal to 2. We especially focus our attention on the effects of the Reynolds number. Three flow cases are examined at friction Reynolds numbers $Re_\tau = \delta_{99}/\delta_v = 500$, 1000 and 2000, based on the properties of the undisturbed boundary layers at the ramp location, where δ_{99} is the boundary layer thickness, $\delta_v = \nu_w/u_\tau$ is the viscous length scale, $u_\tau = \sqrt{\tau_w/\rho_w}$ is the friction velocity, ρ_w and ν_w are the density and kinematic viscosity at the wall, respectively. The topic has been scarcely considered in the literature. In particular, only Giepman *et al.* (2016) described the streamwise evolution of the main features of the mean wake velocity for Reynolds number based on the boundary layer thickness in the range $[4.9 \times 10^5, 10.5 \times 10^5]$ but the results did not show any relevant difference in the interval considered. However, despite the potential importance, no study is available at present concerning the effects of microramps at small or moderate Reynolds numbers.

The paper is organised as follows: § 2 presents the methodology and numerical set-up of the simulations; § 3 describes the database generated and the validation carried out; § 4 presents the results of the analysis; finally, § 5 reports some final comments.

2. Methodology and numerical set-up

The DNS database considered in this work has been generated using STREAmS 2.0 (https://github.com/STREAmS-CFD/STREAmS-2) (Bernardini *et al.* 2021, 2023*b*; Sathyanarayana *et al.* 2023). The open-source finite-difference compressible flow solver, STREAmS, developed by our group, is designed to solve the compressible Navier–Stokes equations for a perfect, heat conducting gas. The solver targets canonical wall-bounded turbulent high-speed flows, and is oriented to modern HPC platforms with the capability to run on both NVIDIA (Bernardini *et al.* 2021, 2023*b*) and AMD (Sathyanarayana *et al.* 2023) GPUs.

The discretisation of the convective terms adopts a hybrid energy-conservative/shock-capturing scheme in locally conservative form (Pirozzoli 2010). In smooth regions, a sixth-order, central, energy-preserving flux formulation ensures stability without the addition of numerical diffusivity. Close to the shock waves, a fifth-order, weighted essentially non-oscillatory (WENO) reconstruction (Jiang & Shu 1996) is used to compute numerical fluxes at the cell faces, using a Lax–Friedrichs flux vector splitting. A shock sensor evaluates the local smoothness of the solution and identifies the regions where discontinuities occur, and where the switch between the central and the WENO scheme takes place. Viscous terms are approximated by means of sixth-order, central finite-difference approximations. Time advancement is carried out by means of a third-order, low-storage, Runge–Kutta scheme (Spalart, Moser & Rogers 1991).

The size of the computational domain adopted for the simulations is $L_x/\delta_0 \times L_y/\delta_0 \times L_z/\delta_0 = 100 \times 15 \times 10$, the reference length δ_0 being the thickness of the boundary layer at the inflow. The microramp geometry for the three flow conditions considered is based on the optimal shape defined by Anderson *et al.* (2006) (see figure 2), with a constant ratio between the ramp height and the boundary layer thickness of the uncontrolled case, $h/\delta_{99} = 2/3$. This configuration has been studied experimentally by Tambe, Schrijer & van Oudheusden (2021), at the same Mach number but at a higher Reynolds number ($Re_\theta = 2.4 \times 10^4$, $Re_\tau \approx 5000$). The microramp is centred in the cross-stream plane, and the ramp trailing edge is $60\,\delta_0$ from the inlet section. The trailing edge of the ramp is also the origin of our reference system. The mesh is uniform in the wall-parallel
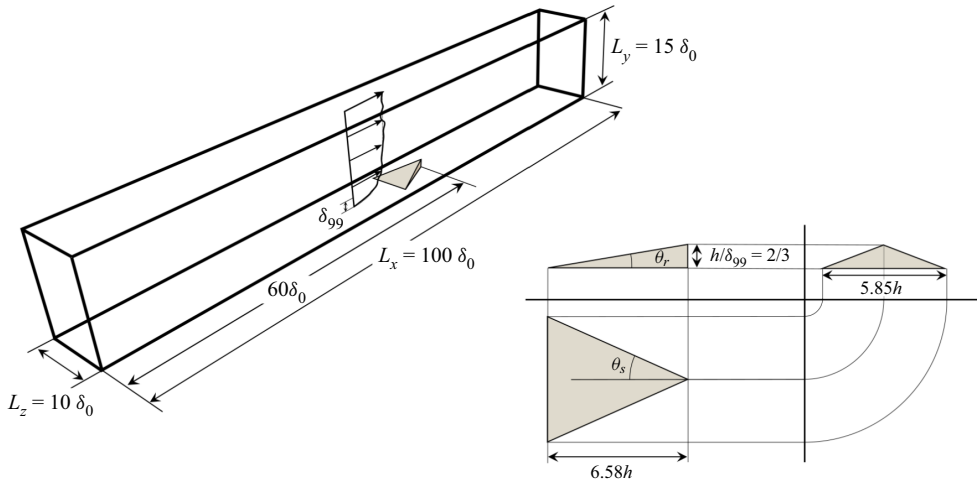
Figure 2. Domain with sizes and orthogonal projections of the microramp.

directions, corresponding to a viscous-scaled spacing of $\Delta x^+ \approx 6.9$ and $\Delta z^+ \approx 5.5$, in the streamwise and spanwise directions, respectively. The mesh is stretched in the wall-normal direction, corresponding to a wall-spacing in the range $\Delta y^+ \approx 0.75$–0.95. The microramp is simulated by means of a ghost-point-forcing immersed boundary method (IBM) (Piquet, Roussel & Hadjadj 2016) already validated in previous works (Modesti *et al.* 2022).

The boundary conditions are specified as follows. At the outflow and the top boundaries, non-reflecting conditions are imposed by performing a characteristic decomposition in the direction normal to the boundaries (Poinsot & Lele 1992). A characteristic wave decomposition is also employed at the bottom no-slip wall, where the wall temperature is set to the recovery value of the incoming boundary layer. In order to prescribe suitable turbulent fluctuations at the inflow, a recycling–rescaling procedure (Lund, Wu & Squires 1998) is used, with a recycling station placed at $50\delta_0$ from the inflow to guarantee a sufficient decorrelation between the inlet and the recycling station. Finally, the flow is assumed to be statistically homogeneous in the spanwise direction, thus periodic boundary conditions are applied on the sides. Hence, simulations are representative of an array of microramps with lateral spacing s such that $s/\delta_0 = L_z/\delta_0 = 10$.

3. Numerical data set and validation

The main parameters of the numerical database analysed in this work are reported in table 1. The data set includes baseline simulations with undisturbed boundary layer, which are used as a reference to assess the effects of the microramps. We consider three values of friction Reynolds number $Re_\tau = 500, 1000, 2000$, based on the properties of the undisturbed boundary layers. The corresponding Reynolds number based on the momentum thickness is reported in table 1 together with the number of mesh points. The free stream Mach number M_∞ is equal to 2 for all the flow cases. In the following, unless otherwise specified, we will indicate with the colours red, blue and black the cases at low, intermediate and high Reynolds number, respectively.

In order to characterise the incoming turbulent boundary layer, figure 3 shows a comparison of the van Driest transformed mean velocity profiles and of the density-scaled Reynolds stress components with the incompressible data from the DNS database of Sillero, Jiménez & Moser (2013). For the case with the highest Reynolds number, an

Case	M_∞	Re_τ	Re_θ	$N_x \times N_y \times N_z$	h/δ_0
UBL – L	2.00	500	2330	$4096 \times 288 \times 512$	—
UBL – M	2.00	1000	4870	$8192 \times 512 \times 1024$	—
UBL – H	2.00	2000	9880	$16\,384 \times 896 \times 2048$	—
MBL – L	2.00	500	2330	$4096 \times 288 \times 512$	1.26
MBL – M	2.00	1000	4870	$8192 \times 512 \times 1024$	1.16
MBL – H	2.00	2000	9880	$16\,384 \times 896 \times 2048$	1.12

Table 1. Main parameters of the numerical database. Reynolds numbers are evaluated at the trailing edge of the microramp. Here UBL, uncontrolled boundary layer; MBL, microramp-controlled boundary layer; L, low Reynolds number; M, intermediate Reynolds number; H, high Reynolds number.
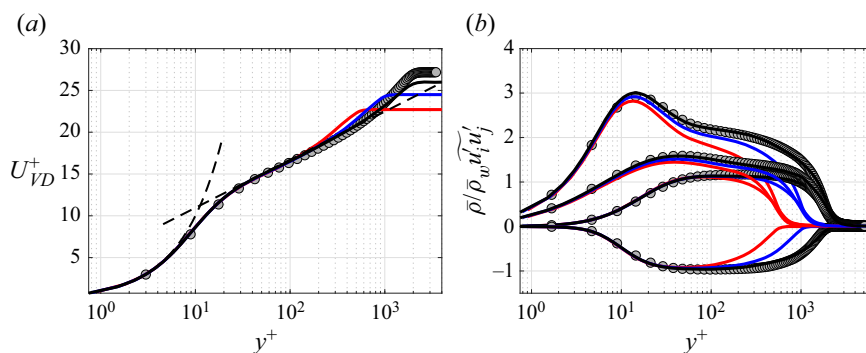

Figure 3. Comparison of (*a*) van Driest transformed mean velocity profile and (*b*) density-scaled Reynolds stress components for the incoming boundary layer with reference experimental data by Sillero *et al.* (2013) (circles, $Re_\tau = 1989$).

excellent agreement can be observed for the mean velocity from the viscous sublayer up to the outer region, where the mean velocity wake departs from the transformed profile slightly. The Reynolds stress components, represented in wall units, are reported instead in figure 3(*b*). Increasing the friction Reynolds number, all the components converge towards the incompressible results.

4. Results

4.1. *Qualitative flow organisation*

First, we describe the qualitative behaviour of the instantaneous flow in terms of turbulent structures, and we outline the organisation of the shock system taking place in the field.

4.1.1. *Turbulent structures*

Figure 4 depicts, for the three controlled cases, the instantaneous turbulent structures identified by means of isosurfaces of the imaginary part of the velocity gradient tensor's complex eigenvalues $\lambda_{ci}h/U_\infty$ (swirling strength criterion (Zhou *et al.* 1999)), coloured by the streamwise velocity component (a supporting video about the fluid field generated by a supersonic turbulent boundary layer impinging on a microramp is available in high resolution at https://youtu.be/o8olmjiWSl8 (Salvadore *et al.* 2022)). First of all, it is possible to observe the fine turbulent structures upstream of the microramp, which become smaller by increasing the Reynolds number. At high Reynolds number, the large-scale streamwise streaks are evident, corresponding to regions of alternating high-
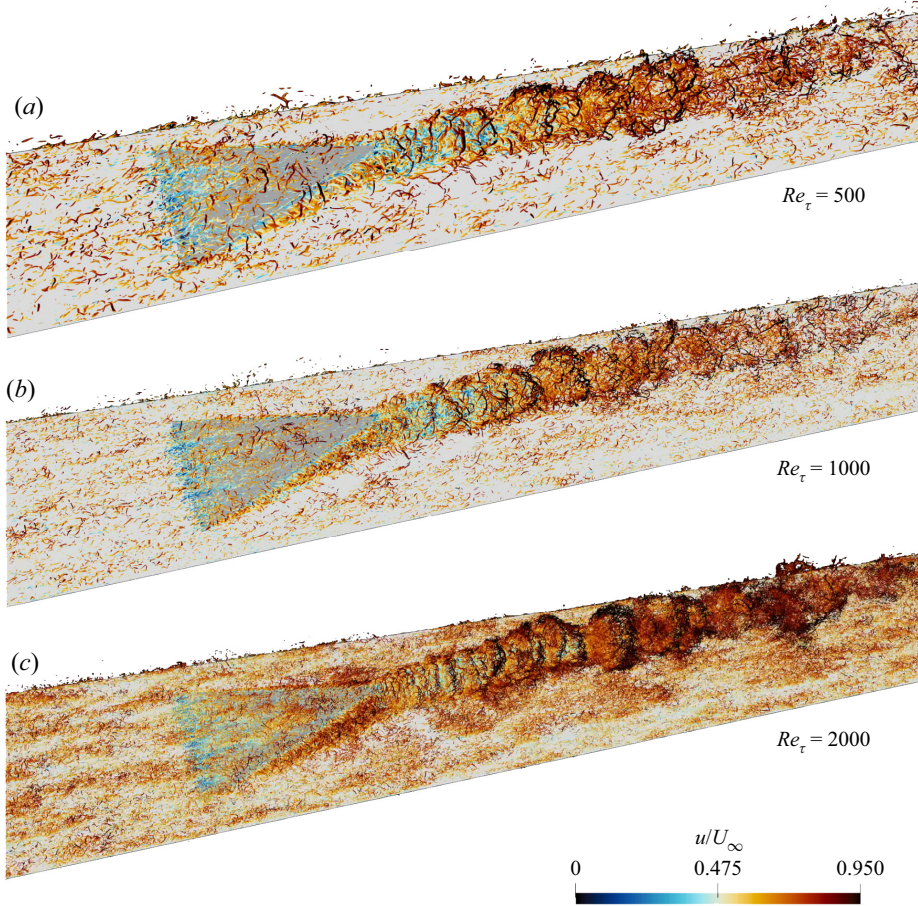
Figure 4. Isosurfaces of the swirling strength coloured by the streamwise velocity component: (*a*) $Re_\tau = 500$ ($\lambda_{ci}h/U_\infty = 3.2$); (*b*) $Re_\tau = 1000$ ($\lambda_{ci}h/U_\infty = 5.1$); (*c*) $Re_\tau = 2000$ ($\lambda_{ci}h/U_\infty = 7.1$).

and low-speed flow. When the flow encounters the ramp, the slope of the top surface induces a first shock that generates a small region with reduced velocity at the foot of the ramp. On the top ramp surface, the flow accelerates as streamlines are forced to converge, then the flow deflects laterally and diverges towards the sides of the ramp, up to its edges. From here, the accelerated flow leaves the top surface and naturally generates the primary vortices on the sides of the ramp, together with smaller secondary vortices close to the top and bottom edges. The primary vortices increase in strength and radius proceeding downstream until they converge on the trailing edge of the ramp where they deflect, becoming nearly parallel and aligned with the streamwise direction. The convergence of the primary vortex pair and the accelerated flow from the top edge of the ramp initiate vortex roll-up in the arc region above the primary vortices. Soon after the edge of the ramp, arc-shaped vortical structures are distinguishable in all the three cases, especially for higher Reynolds numbers. In accordance with the model proposed by Sun *et al.* (2014*b*), the lift-up of the wake and the entrainment of lateral flow in the near-wall region tend to close the arc-shaped structures into almost-toroidal vortex rings that enclose the decaying primary vortex pair. Vortex rings are then convected downstream and, together with the primary vortex pair inside, induce velocity fluctuations that are responsible for the meandering and, eventually, the breakdown of the wake.
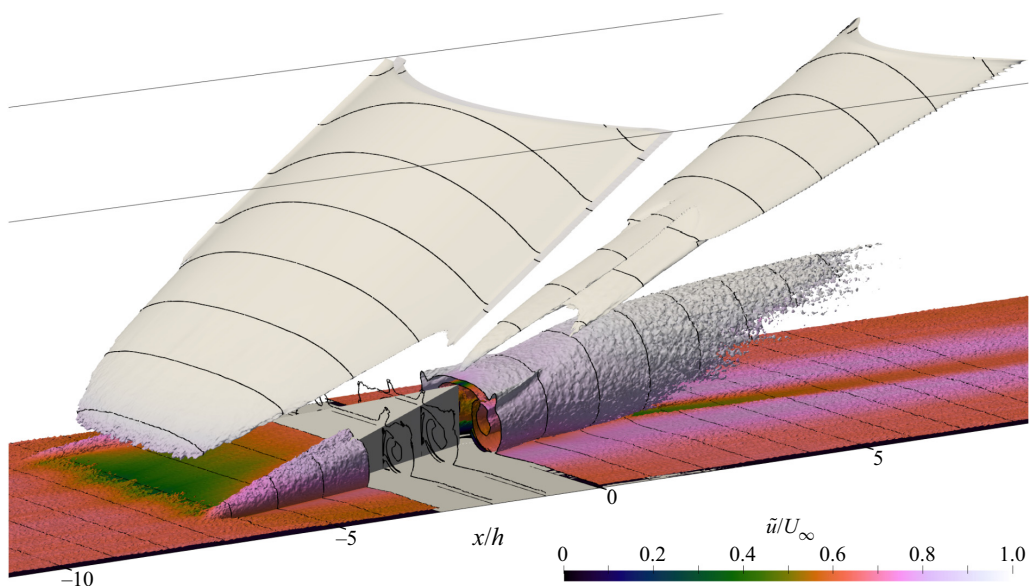
Figure 5. Isosurface of the magnitude of the mean density gradient ($\|\boldsymbol{\nabla}\rho\delta_0/\rho_\infty\| = 0.25$), coloured by the streamwise velocity component. Vertical yz slices of the surface, spaced by h, highlight the 3-D shape of the shocks, whereas the isosurface at the trailing edge region is hidden to show the internal convolution of the primary vortices.

4.1.2. *Shock system*

Besides the highlighted vortical structures, a series of complex, 3-D shocks is also generated in the field as a consequence of the numerous changes in direction of the supersonic flow around the ramp. To better understand the complex structure of the shocks, we report in figure 5 an isosurface of the magnitude of the mean density gradient, coloured by the streamwise velocity for the intermediate Reynolds number. Slices of the isosurface at constant *x* help us to understand its 3-D curvature and the interior structure of the field. Figure 6, instead, shows the gradient of the mean density in logarithmic scale on several planes at constant *x* from two different 3-D views and on a wall-parallel plane at $y/h = 5.7$. For symmetry reasons, only half of the domain is shown. Time averaging is conducted over a period of approximately $340h/U_\infty$.

We note that the density gradient is able to highlight better the shocks and the dominant vortical structures delimiting the wake. As mentioned above, the slope of the MVG induces a first shock from the foot of the ramp, which we will refer to as foot shock. Since the ramp has a finite extension, the originally planar foot shock must curve in the spanwise direction while evolving in the longitudinal direction, as can be seen from its curvature on the top of the domain.

After the foot shock, in the final region of the developing primary vortices at the sides of the ramp, we observe the formation of an oblique shock wave inclined at approximately $45°$ right on top of the vortices. These shocks, which we will refer to as vortex shocks, are stronger for flow cases at higher Reynolds numbers. Although in part related to the reduced viscous dissipation, we will discuss in § 4.2.1 that if the ramp geometry is fixed with respect to the height of the boundary layer, increasing Reynolds number leads to an increase in the circulation of the vortex pair and in the velocity magnitude of the flow
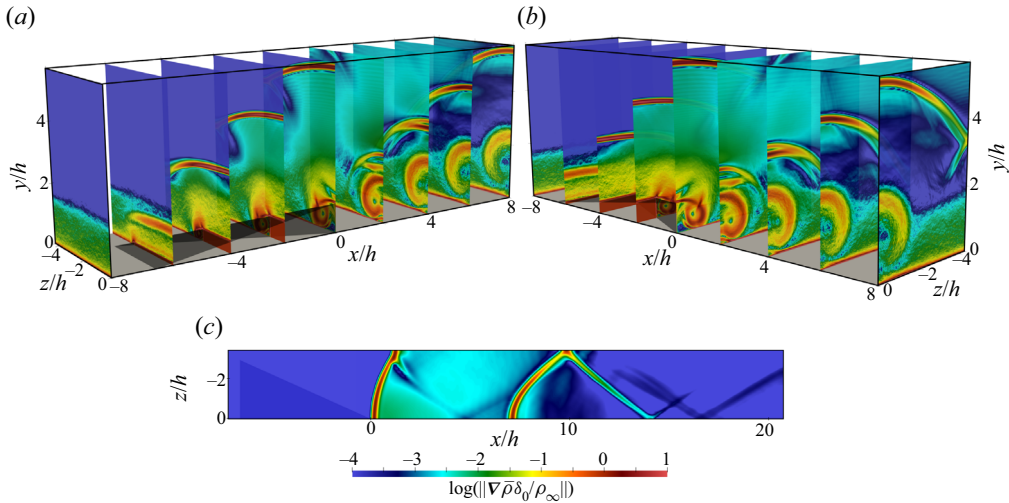
Figure 6. Contours of the non-dimensional mean density gradient in logarithmic scale on several yz transparent planes at different streamwise locations spaced by $2h$ (a,b) and on a xz plane at $y/h = 5.7$ (c). Only half of the domain is shown for symmetry.

captured in the side vortices in general, which increases the strength of the compression in the end.

At the trailing edge of the ramp, the flow on the top surface undergoes an initial vertical deflection in the central plane induced by the converging primary vortices, giving rise to a shock from the ramp main edge. This flow deflection is significant only in the trailing edge region close to the symmetry plane, whereas it decreases laterally, thus resulting in a conical shock. Slightly downstream of the ramp trailing edge, the increased lift-up generated by the mutual interaction of the primary vortex pair develops fully and pushes the wake further up, inducing a second shock. We will refer to these shocks as the trailing edge shocks. Given the topology of the foot shock and the spanwise variation of the flow deviation, the trailing edge shocks also have a conical shape, as can be seen from the slice in the xz plane at the top of the computational domain. After less than one ramp length, the two trailing edge shocks coalesce. Below the conical compression, it is possible to appreciate the development of the primary vortex pair, with two distinct convoluted vortices just after the ramp trailing edge. Proceeding downstream, the diffusion and the entrainment of flow from outside of the wake enlarges the cores of the vortices and 'unroll' the inner convolution: after slightly more than one ramp length from the main edge, the low-momentum region has an almost circular shape. Finally, we also observe the shocks coming from the side ramps outside of the computational domain, as a result of the periodic boundary conditions.

In order to obtain a clearer picture of the shock system, we also report three contours of the instantaneous density in the xy planes at $z/h = -0.5L_z/h$, $-0.5b/h$ and 0 for the case at high Reynolds number, where b is the spanwise half-width of the ramp (figure 7). At the side surfaces of the domain, it is possible to see only the foot shock and the trailing edge shock. From the intermediate spanwise position, we can observe the significant compression induced by the foot shock. The core of the primary vortex is then highlighted by the region with low density close to the edge of the ramp. Slightly after, on top of the trace of the primary vortex pair, the trailing edge shock occurs, followed by a milder compression due to the shock coming from the side ramps. Farther downstream,
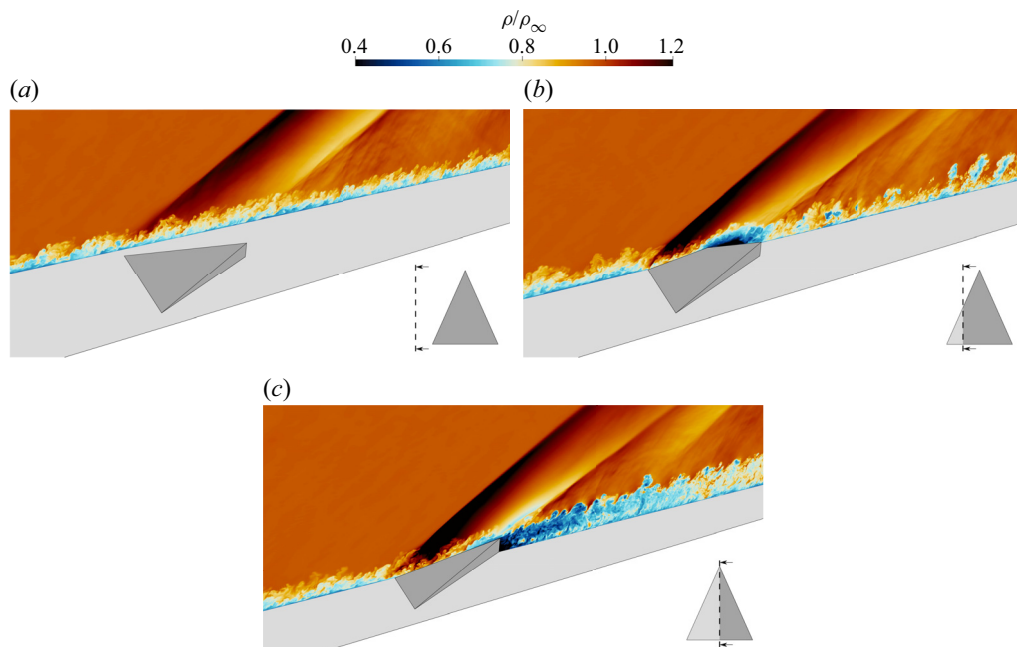
974 A44-10

Figure 7. Contours of the instantaneous density on vertical slices at different spanwise sections: (*a*) lateral wall ($z/h = -0.5L_z/h$); (*b*) intermediate spanwise location ($z/h = -0.5b/h$); (*c*) centre of the ramp ($z/h = 0$). Low Reynolds number case.

low-density regions suggest the presence of the vortex rings observed in figure 4. Finally, the slice at the symmetry plane of the ramp shows all the main shocks of the flow field clearly. The foot shock and the trailing edge shocks have here their maximum intensities, and behind the trailing edge shocks, the shock stemming from the side ramp is also visible. The instantaneous density on this plane also makes evident how, after fewer than two ramp heights, KH instabilities generate vortical structures over the primary vortices, with cores highlighted by spots of reduced density.

Concerning the effect of the Reynolds number on the shock structure, a comparison between the cases did not reveal relevant qualitative differences with respect to the described picture.

4.2. *Streamwise evolution of the wake*

In the following, we discuss various aspects concerning the streamwise development of the wake, focusing in particular on the Favre-averaged streamwise and vertical velocity components, for which also experimental data are available. Favre-averaging of a generic variable f is indicated with the tilde and is defined as $\tilde{f} = \overline{\rho f}/\bar{\rho}$, where the bar indicates Reynolds-averaging instead.

4.2.1. *Wall-normal profiles of velocity on the symmetry plane*

Figure 8 shows the velocity profiles on the symmetry plane at $x/h = 10.7$ for the three different Reynolds numbers, together with the corresponding uncontrolled cases and the experimental results of Tambe *et al.* (2021). From the streamwise velocity component $\tilde{u}/U_\infty$ in figure 8(*a*), it is evident that for increasing Re_τ, the microramp is more efficient,
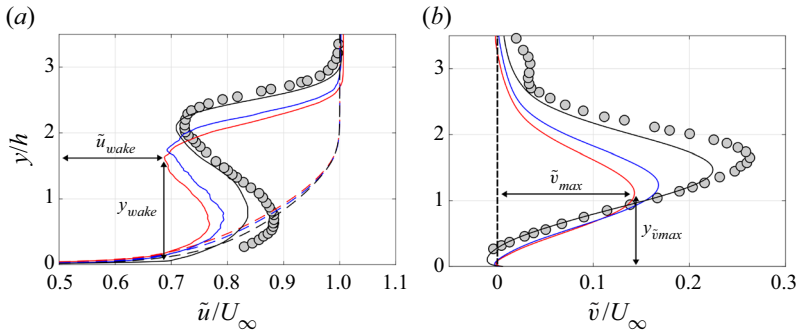
Figure 8. Velocity profiles at $x/h = 10.7$: (*a*) streamwise and (*b*) wall-normal components. Dashed lines denote the velocity profiles in undisturbed conditions. Symbols denote experiments by Tambe *et al.* (2021) (circles, $M_\infty = 2.0$, $Re_\theta = 2.4 \times 10^4$): (red lines) $Re_\tau = 500$; (blue lines) $Re_\tau = 1000$; (black lines) $Re_\tau = 2000$.

and is thus able to produce fuller streamwise velocity profiles in the near-wall region (see also § 4.4).

Moreover, the region in the wake characterised by low momentum with respect to the undisturbed profiles rises to higher relative wall-normal locations. An explanation of this phenomenon is given by the profiles of the wall-normal velocity reported in figure 8(*b*), where peak values of $\tilde{v}/U_\infty$ increase markedly with the Reynolds number. The numerical results of both the velocity components tend to the experimental results of Tambe *et al.* (2021), which have been performed at $Re_\tau \approx 5000$.

Observing the longitudinal and vertical components of the velocity at four sections on the symmetry plane in figure 9, we appreciate the lifting up effect on the wake due to the longitudinal primary vortex pair. The trace of the shock wave generated by the microramp trailing edge is also visible in the profiles at section $x/h = 5$. Farther downstream from the microramp, the profiles of both velocity components tend to return to the undisturbed conditions due to the turbulent mixing and flow entrainment from outside the wake.

The increased vertical velocity at the symmetry plane suggests that the circulation of the two parallel primary vortices increases with the Reynolds number. Following for example the approach used in Mole, Skillen & Revell (2022), the velocity field in the yz plane produced by the primary vortex pair from a microramp can be modelled schematically by means of a couple of counter-rotating Batchelor vortices (Batchelor 1964), with two additional mirror vortices with opposite circulation below the wall, to impose wall impermeability, and a linear damping of the azimuthal velocity close to the wall, to impose a no-slip condition. The azimuthal velocity V_θ of an isolated Batchelor vortex is defined as

$$V_\theta(r) = \frac{qR}{r}\left[1 - \exp\left(-\frac{r^2}{R^2}\right)\right] \tag{4.1}$$

where q is the vortex strength, r is the distance from the centre of the vortex and R is the radius of the vortex core. Figure 10(*a*) shows only the vertical motion induced by a toy model with two parallel vortices of constant circulation on a slice at constant x for two cases where the vortex strength – and hence the circulation – is increased ($q_2/q_1 = 1.25$). Except for the confinement induced by the trailing edge shocks and for the overall downward motion induced by the 3-D flow organisation at the observed station (which makes the DNS results more 'greenish'), the distribution is very similar to the one
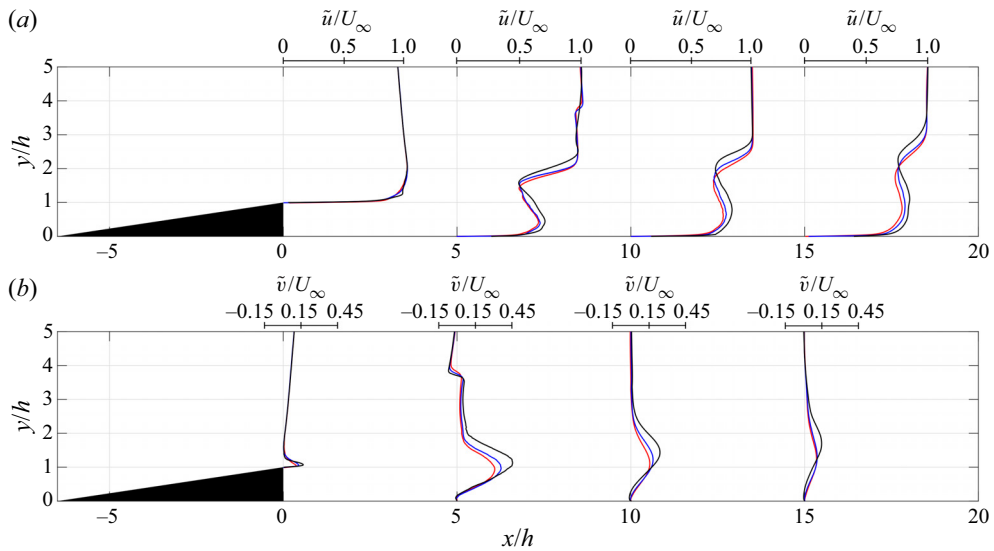
974 A44-12

Figure 9. Streamwise evolution of the velocity profile at four different stations $x/h = 0, 5, 10, 15$: (*a*) streamwise component and (*b*) wall-normal component. (Red lines) $Re_\tau = 500$, (blue lines) $Re_\tau = 1000$; (black lines) $Re_\tau = 2000$.
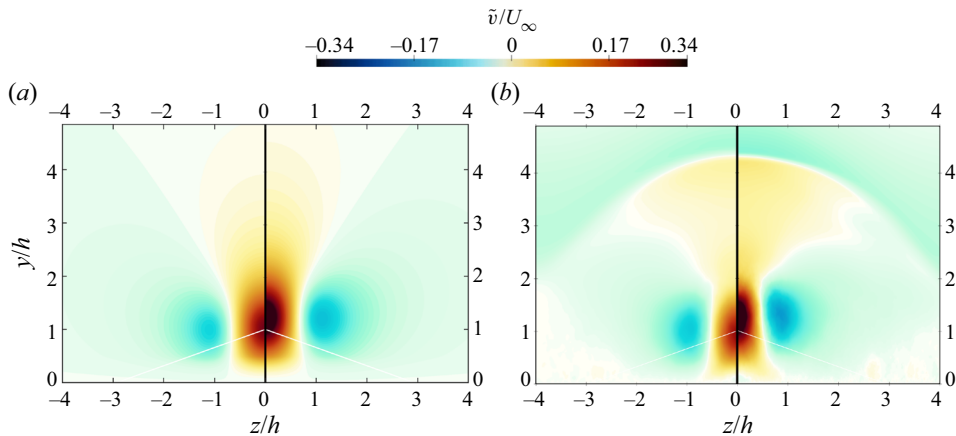

Figure 10. Analytical and numerical vertical velocity. (*a*) Field generated by two parallel Batchelor vortices on a *yz* plane. Vortex strength q_1 at negative *z*, vortex strength $q_2 \approx 1.25q_1$, at positive *z*. (*b*) Favre-averaged vertical velocity at $x/h = 6$ for low (negative *z*) and high (positive *z*) Reynolds numbers simulations.

observed in the wake of the simulated cases reported in figure 10(*b*), confirming that the toy model is able to reasonably represent the real case. From the comparison, we note that the effect of increasing the Reynolds number in the numerical simulations is equivalent to increasing the circulation in the analytical model.

4.2.2. *Boundary layer thickness and shape factor*
In order to evaluate the global properties of the boundary layer before and after the microramp, at the symmetry plane, we use the incompressible displacement and
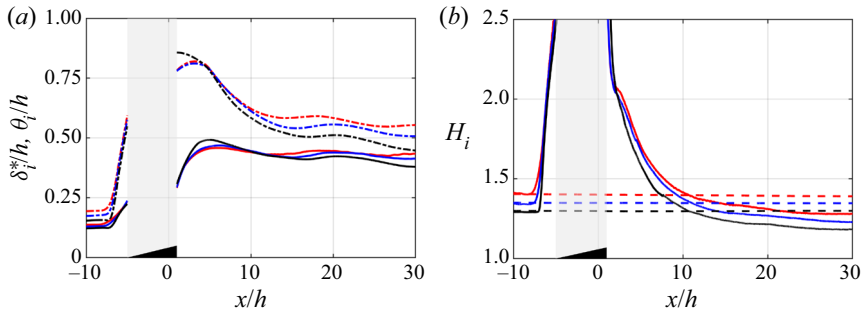
Figure 11. Streamwise evolution of (*a*) boundary layer displacement thickness (dash-dotted lines), momentum thickness (solid lines) and (*b*) incompressible shape factor for the uncontrolled case (dashed lines) and with the microramp (solid lines): (red lines) $Re_\tau = 500$; (blue lines) $Re_\tau = 1000$; (black lines) $Re_\tau = 2000$.

momentum thicknesses,

$$\delta_i^* = \int_0^\infty \left(1 - \frac{\tilde{u}}{U_\infty}\right) \mathrm{d}y \quad \text{and} \quad \theta_i = \int_0^\infty \frac{\tilde{u}}{U_\infty} \left(1 - \frac{\tilde{u}}{U_\infty}\right) \mathrm{d}y \qquad (4.2a,b)$$

which are reported in figure 11(*a*). Both δ_i^* and θ_i grow remarkably after the microramp, but at different rates, and thus the incompressible shape factor $H_i = \delta_i^*/\theta_i$ becomes lower than the upstream condition and also than the uncontrolled cases (figure 11*b*), indicating fuller boundary layers close the wall, which would be less prone to separation in the presence of SBLIs.

4.2.3. *Wake velocity and maximum upwash*

Another key element in the control efficiency of microramps is the strength and decay of the low-momentum deficit in the wake. In fact, in addition to the vertical motion induced by the primary vortices, the continuous entrainment of fluid with higher momentum from outside the wake, the interaction between the toroidal vortical structures and the primary vortex pair, and the effect of viscous and turbulent dissipation, gradually enlarge and restore the region with low momentum, leading the wake to disappear after some distance from the ramp.

The wake development along the x direction is typically analysed by considering the following quantities on the basis of the vertical velocity profiles at the symmetry plane (Giepman *et al.* 2016): the wake velocity $\tilde{u}_{wake}$, defined as the minimum streamwise velocity in the low momentum region, and its corresponding vertical position y_{wake}; the maximum upwash velocity $\tilde{v}_{max}$ and its vertical position $y_{\tilde{v}max}$ (see figure 8).

Babinsky *et al.* (2009) reported the streamwise evolution of the momentum deficit on several cross-stream planes and, inspired by the work of Ashill, Fulker & Hackett (2005) in the incompressible regime, hypothesised that the flow development varies with the height of the device (for fixed boundary layer thickness). To test this hypothesis for geometrically similar ramps with different heights, the authors reported the wake location as a function of the streamwise distance from the main edge, both normalised with the ramp height. The collapse between the curves of the different cases, later confirmed also by other studies (Giepman *et al.* 2014), indicated that, at least for similar inflow conditions, the ramp height is able to scale the wake features successfully. For this reason, in the following, we try also in our case to scale wake lengths by the ramp height h.

Figure 12(*a*) shows that the streamwise evolution of $\tilde{u}_{wake}$, normalised by the undisturbed velocity U_∞, collapses reasonably on a single curve for the three cases,
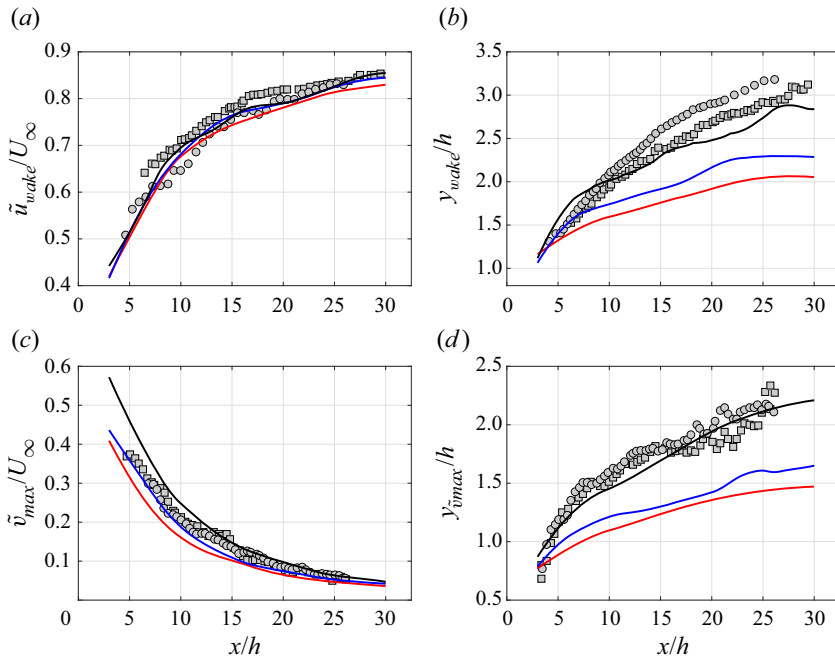
974 A44-14

Figure 12. Streamwise evolution of (*a*) wake velocity and (*b*) wake location, (*c*) maximum upwash velocity, (*d*) maximum upwash location for different Re_τ, scaled by h. Symbols in (*a,b*) denote experiments by Tambe *et al.* (2021) (circles, $M_\infty = 2.0$, $Re_\theta = 2.4 \times 10^4$) and by Giepman, Schrijer & van Oudheusden (2014) (squares, $M_\infty = 2.0$, $Re_\theta = 2.1 \times 10^4$). Symbols in (*c,d*) denote experiments by Giepman *et al.* (2016) (circles, $M_\infty = 2.0$, $Re_\theta = 5.0 \times 10^4$ and squares, $M_\infty = 2.0$, $Re_\theta = 9.9 \times 10^4$): (red lines) $Re_\tau = 500$; (blue lines) $Re_\tau = 1000$; (black lines) $Re_\tau = 2000$.

following the experimental results of Tambe *et al.* (2021) and Giepman *et al.* (2014). The wake position is much more sensitive to the Reynolds number and numerical results converge towards the experimental ones only for the case at high Reynolds number, which suggests that after a certain threshold the flow becomes independent of the Reynolds number. A similar trend is also observed for the wall-normal upwash velocity $\tilde{v}_{max}$ and its location in figures 12(*c*) and 12(*d*).

4.2.4. *Self-similarity of velocity profiles*

In this section, we also examine the self-similarity of the velocity profiles following the formulation proposed by Sun *et al.* (2014*b*). For the profiles of the streamwise component, the velocity is normalised by the quantity $\Delta\tilde{u}_{deficit}$, defined as the maximum difference between the velocity profile of the controlled case and that of the undisturbed boundary layer u_{BL}, while the vertical coordinate is normalised by the wake location y_{wake}. Thus, we have that

$$\hat{U}(\eta_u) = \frac{\tilde{u}(\eta_u) - u_{BL}(\eta_u)}{\Delta\tilde{u}_{deficit}}, \quad \eta_u = \frac{y - y_{wake}}{y_{wake}}. \quad (4.3a,b)$$

On the other hand, for the wall-normal component, the velocity is normalised by the maximum upwash velocity $\tilde{v}_{max}$, while the vertical coordinate is normalised by $y_{\tilde{v}max}$,
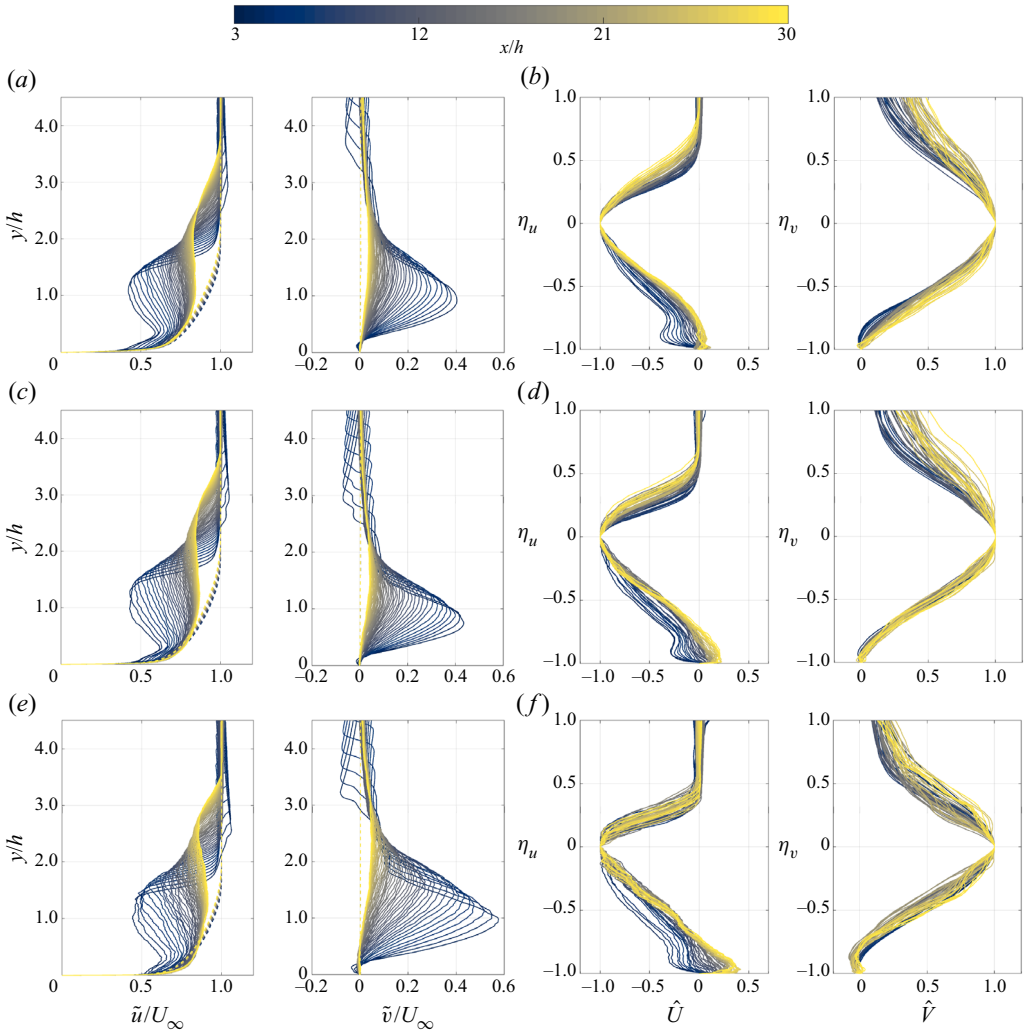
Figure 13. Velocity profiles at: (*a,b*) $Re_\tau = 500$, (*c,d*) $Re_\tau = 1000$, (*e,f*) $Re_\tau = 2000$. Non-normalised (*a,c,e*) and normalised (*b,d,f*) streamwise and wall-normal velocity. Colour indicates the streamwise location according to the colourbar. Dashed lines indicate the uncontrolled boundary layer.

so that

$$\hat{V}(\eta_v) = \frac{\tilde{v}(\eta_v)}{\tilde{v}_{max}}, \quad \eta_v = \frac{y - y_{\tilde{v}max}}{y_{\tilde{v}max}}. \tag{4.4a,b}$$

As also demonstrated by Sun *et al.* (2020), velocity profiles exhibit self-similarity, especially in the central region of the wake, whereas discrepancies are expected in the near wake and in the near-wall region, where the bottom secondary vortices induce a region of low velocity, and flow reversal can also occur.

The normalised velocity profiles at several equispaced streamwise locations in the region $x/h = 3$ to $x/h = 30$ are shown in figure 13. A very good agreement is observed for the scaled profiles, which is quantified in figure 14 by reporting the streamwise average of the
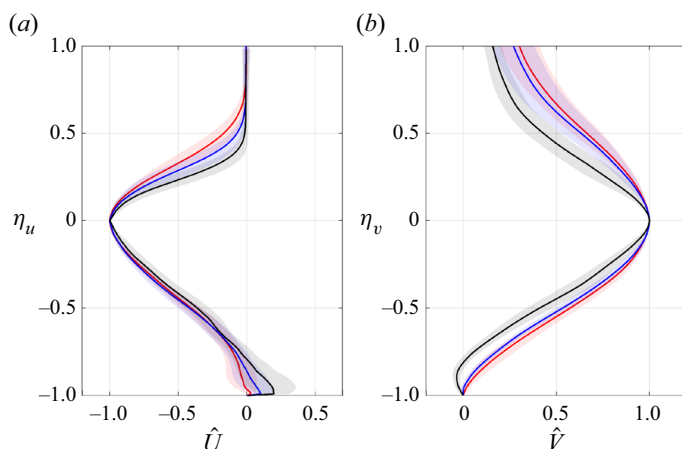
974 A44-16

Figure 14. Normalised velocity profiles for different Re_τ: (*a*) streamwise component and (*b*) wall-normal component. The normalised profiles are averaged in the streamwise direction. Banded regions indicate the corresponding standard deviation from the streamwise-averaged profile. (Red lines) $Re_\tau = 500$, (blue lines) $Re_\tau = 1000$, (black lines) $Re_\tau = 2000$.

scaled profiles along with the corresponding standard deviation, for the three Reynolds numbers.

Excluding the very near-wall region where viscous effects are dominant, the maximum standard deviation for the streamwise velocity component $\sigma_{\hat{U}}$ is 0.078, 0.082, 0.091 for the low, intermediate and high Reynolds numbers, respectively, which confirms that $\tilde{u}$ is self-similar. Differences among the three flow cases are also of the same order of the standard deviation, and therefore are considered satisfactory.

Regarding the normalised vertical velocity profiles, minor deviations are visible in the lower region of the wake, and the standard deviation is generally very small. Vertical self-similarity is more troublesome to infer in the upper part of the wake and has a different behaviour especially for higher Reynolds number. In particular, the outer region is also influenced by the trailing edge shock, and thus perfect self-similarity is difficult to achieve. Additionally, the increased lift-up and the faster rise of the wake for the higher Reynolds number case is strong enough to induce a region of negative $\tilde{v}$ at the symmetry plane (see figure 10*b*), which further aggravates the differences with respect to the other two cases.

4.3. *Mean wake organisation*

In the following, we consider the evolution of the time-averaged flow quantities in the very near ($x/h < 2$) and far wake ($x/h > 4$) behind the microramp.

4.3.1. *The near wake*

We have seen in the previous sections that the captured flow from the incoming boundary layer generates two symmetric vortical structures at the sides of the ramp, which converge at the trailing edge and then proceed approximately in parallel. The behaviour and decay of the primary vortex pair far from the edge has been widely considered in several experimental studies (Giepman *et al.* 2014, 2016; Sun *et al.* 2014*b*; Tambe *et al.* 2021), and although some aspects still remain unclear, several studies provided valuable insights into the development of the far wake.

On the other hand, less is known about the near wake, as this region is difficult to study experimentally due to the presence of the solid walls. Despite its reduced extent, in this critical region important changes take place that influence the evolution of the entire wake downstream. In order to draw a qualitative picture of the flow in the near wake, we report in figure 15 the Favre-averaged streamwise velocity component and the three orthogonal components of the Favre-averaged vorticity ζ on equispaced cross-stream planes in the region $x/h \in [-0.4, 2]$ for the flow case at intermediate Reynolds number. White isolines indicate a constant value of the density gradient, highlighting the edges of the main vortices and shocks, as reported in figure 6. Due to symmetry, only half of the domain is reported and discussed.

The velocity field in figure 15(*a*) clearly highlights the core of the primary vortex, from which we can infer its internal organisation. Close to the wall and the symmetry plane, especially near the trailing edge of the ramp as shown in the zoomed region, we note an extended region of low-speed reversed flow, corresponding to a small separation and a near-wall secondary vortex. This region shrinks progressively downstream and flow reversal is almost absent at the end of the considered interval. The isolines of the density gradient on top of the main vortex show the oblique shock on the side vortex propagating downstream and disappearing approximately one *h* from the ramp. The isoline of the density gradient also highlights the spreading and internal convolution of the main vortex, represented by the negative values of ζ_1 in figure 15(*b*).

The distributions of the wall-normal and spanwise vorticity components in figure 15(*c*,*d*) complements the understanding of the above-described vortices. In particular, before the main edge, the two components help us to understand the orientation of the primary and secondary vortices and are able to highlight the internal convolution of the side vortices, superposed to the main streamwise helical motion. After the main edge, where secondary vortices become less important, the transversal components ζ_2 and ζ_3 are particularly useful to capture the trace of the vortical structures inside the wake.

On the basis of the behaviour of the observed quantities, in figure 16 we propose a qualitative description summarising the evolution of the vortical structures in the near wake ($x/h \in [0.4, 2]$). Before the trailing edge, the presence of the vertical lateral wall of the ramp and the inclination of the primary vortices imposes the formation of two asymmetric secondary vortices rotating in the opposite direction of the primary vortices. As soon as the fluid from the top of the ramp flows over the converging vortex pair, the strong shear induces the roll-up of KH instabilities. The KH vortices on top of the wake thus join laterally the counter-rotating helical motion of the two primary vortices, and the typical almost-toroidal vortices are generated as a result. Given its reduced intensity and the significant activity in the top part of the wake, the upper secondary vortex first moves upwards and laterally, following the rotation of the primary vortex, and then disappears soon after the ramp. The bottom secondary vortex instead persists for a longer distance. However, once the primary vortices align and the mutual interaction between them is fully established, the upward vertical motion in between the vortex pair reduces drastically the intensity of the bottom vortex.

While the wake expands, the lift-up in the central region also affects the internal convolution of the primary vortices. The combined distributions of ζ_2 and ζ_3 makes it possible to identify an internal ring-like structure with tangential vorticity oriented in the opposite direction compared with the external almost-toroidal vortices. This structure is superposed to the primary vortices and is progressively pushed upwards by the increased vertical motion induced by the primary vortex pair. In the space where the wake gradually starts to lift up, the intensity of these internal structures decreases and, as a result, there is
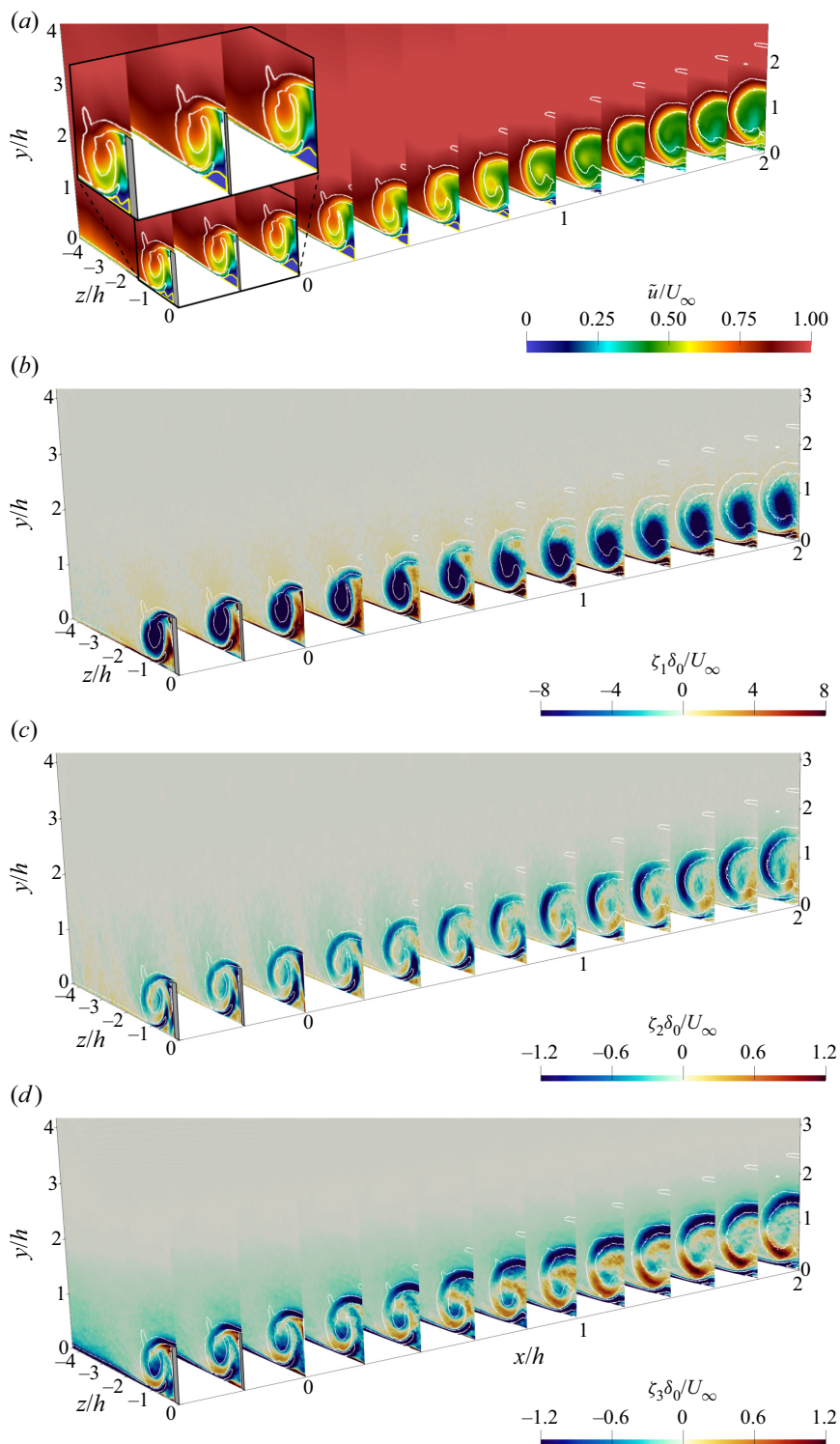
Figure 15. Vertical slices at $x/h \in [-0.4, 2]$ for the case at intermediate Reynolds number. Favre-averaged: (*a*) streamwise velocity; (*b*) streamwise; (*c*) wall-normal; (*d*) spanwise vorticity components. White lines indicate the points with $||\nabla \rho \delta_0 / \rho_\infty|| = 0.25$, while yellow lines in (*a*) and its zoomed region indicate the points with $\tilde{u}/U_\infty = 0$.
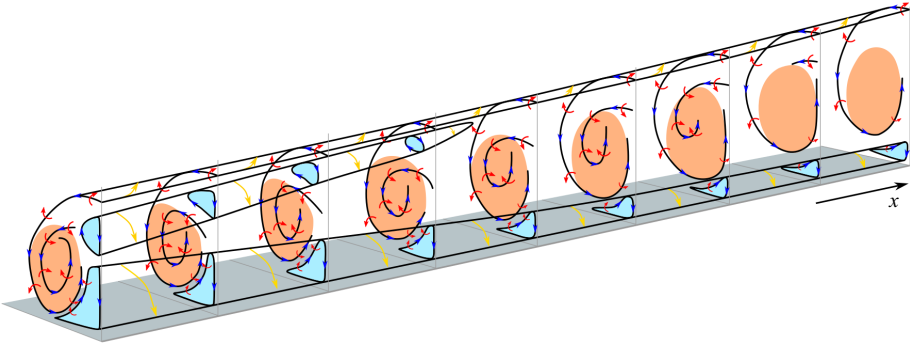
Figure 16. Model sketch of the vortical structures in the near wake ($x/h \in [0.4, 2]$). Yellow arrows indicate the orientation of the helical flow in the primary and secondary vortices; blue arrows indicate the flow rotation in the *yz* planes; red arrows indicate the orientation of the transversal rotation of the vortical structures superposed to the main helical motion; black lines indicate the approximate boundaries of the primary, secondary and inner vortices. Finally, the region with negative (positive) streamwise vorticity related to the primary vortex (secondary vortices) is indicated in orange (light blue).

no evident sign of them after less than $2h$ from the ramp trailing edge anymore. Close to the symmetry plane, on the other hand, convolution is still visible from ζ_2 (around $z/h \approx -0.5$ in figure 15c), consistently with the observations of secondary vortices inside the wake in the PIV measurements of Sun *et al.* (2012) and in the numerical results of Sun *et al.* (2014a). Contrary to what is proposed by Sun *et al.* (2014a), however, our observations suggest that the 'curved legs' of the KH vortices are already present from the start and are a consequence and evolution of the initial convolution of the primary vortices. Only far from the ramp (approximately $x/h > 15$), the tangential vorticity of the inner, vertical legs is almost completely dissipated and only a mild trace is visible inside the wake from ζ_2 close to the symmetry plane. This suggests that in the first part of the wake, the KH vortices are not closed near the wall but are instead strictly tied to the helical motion of the primary vortices they surround. A stricter closure of the tangential vorticity takes place only far downstream, where instead we observed a significant decrease in coherence of the azimuthal structures (see figure 4), at least at the present Reynolds numbers.

4.3.2. *The far wake*

Once the primary vortices become parallel and the wake starts to lift up, the low-momentum region spreads and the intensity of the wake deficit progressively decays. In order to describe the evolution of the wake far from local effects due to the presence of the ramp, we report in figure 17 the behaviour of the Favre-averaged Mach number ($\tilde{M} = \sqrt{\tilde{u}^2 + \tilde{v}^2 + \tilde{w}^2}/\sqrt{\gamma R \tilde{T}}$), and of the Favre-averaged Reynolds stress components $\widetilde{\tau_{11}} = -\overline{\rho u'' u''}$, $\widetilde{\tau_{22}} = -\overline{\rho v'' v''}$, $\widetilde{\tau_{33}} = -\overline{\rho w'' w''}$, $\widetilde{\tau_{12}} = -\overline{\rho u'' v''}$, where the symbol $(\bullet)''$ indicates the fluctuations of a variable with respect to its Favre average. The figure shows the above-mentioned quantities on three *yz* slices at $x/h = 4$, 8 and 16, for the intermediate Reynolds case only. Since we observed decay properties similar to the $\widetilde{\tau_{12}}$ component for the other two transversal components, $\widetilde{\tau_{13}}$ and $\widetilde{\tau_{23}}$, we do not report them in this figure and we report only their distributions at $x/h = 8$ (figure 18).

The distributions of the temperature and of the Mach number highlight the wake region behind the microramp, which is initially characterised by subsonic conditions, given the lower velocity – and the higher temperature – experienced by the momentum deficit area.
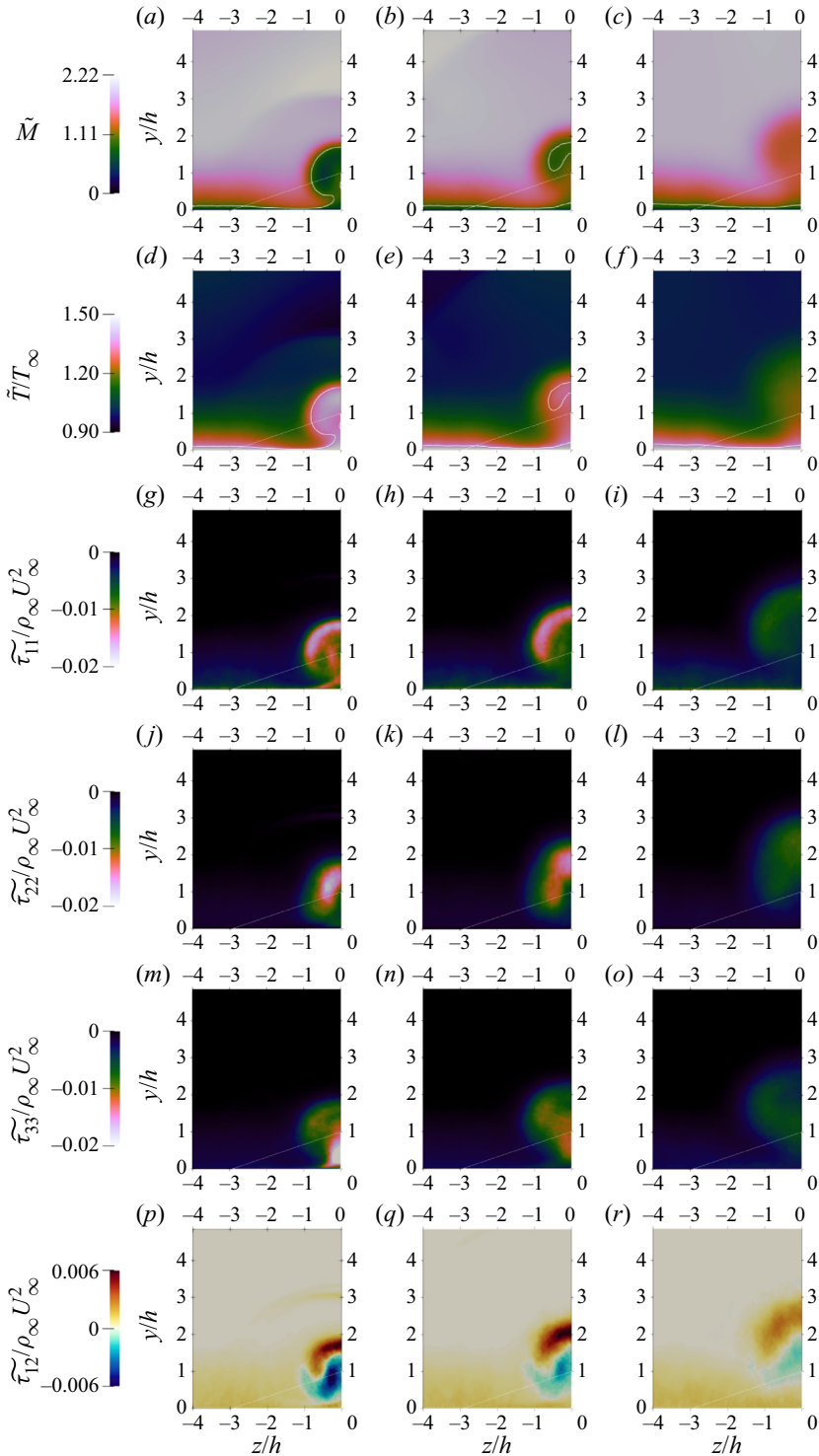
Figure 17. Contours for the intermediate Reynolds number case at $x/h = 4$ (a,d,g,j,m,p), 8 (b,e,h,k,n,q) and 16 (c,f,i,l,o,r) of Favre-averaged Mach number $\tilde{M}$ $(a–c)$, Favre-averaged temperature $\tilde{T}/T_\infty$ $(d–f)$ and Favre-averaged Reynolds stress components $\widetilde{\tau_{11}}/\rho_\infty U_\infty^2$ $(g–i)$, $\widetilde{\tau_{22}}/\rho_\infty U_\infty^2$ $(j–l)$, $\widetilde{\tau_{33}}/\rho_\infty U_\infty^2$ $(m–o)$, $\widetilde{\tau_{12}}/\rho_\infty U_\infty^2$ $(p–r)$. White isolines in the Mach and temperature contours indicate the points with $\tilde{M} = 1$.
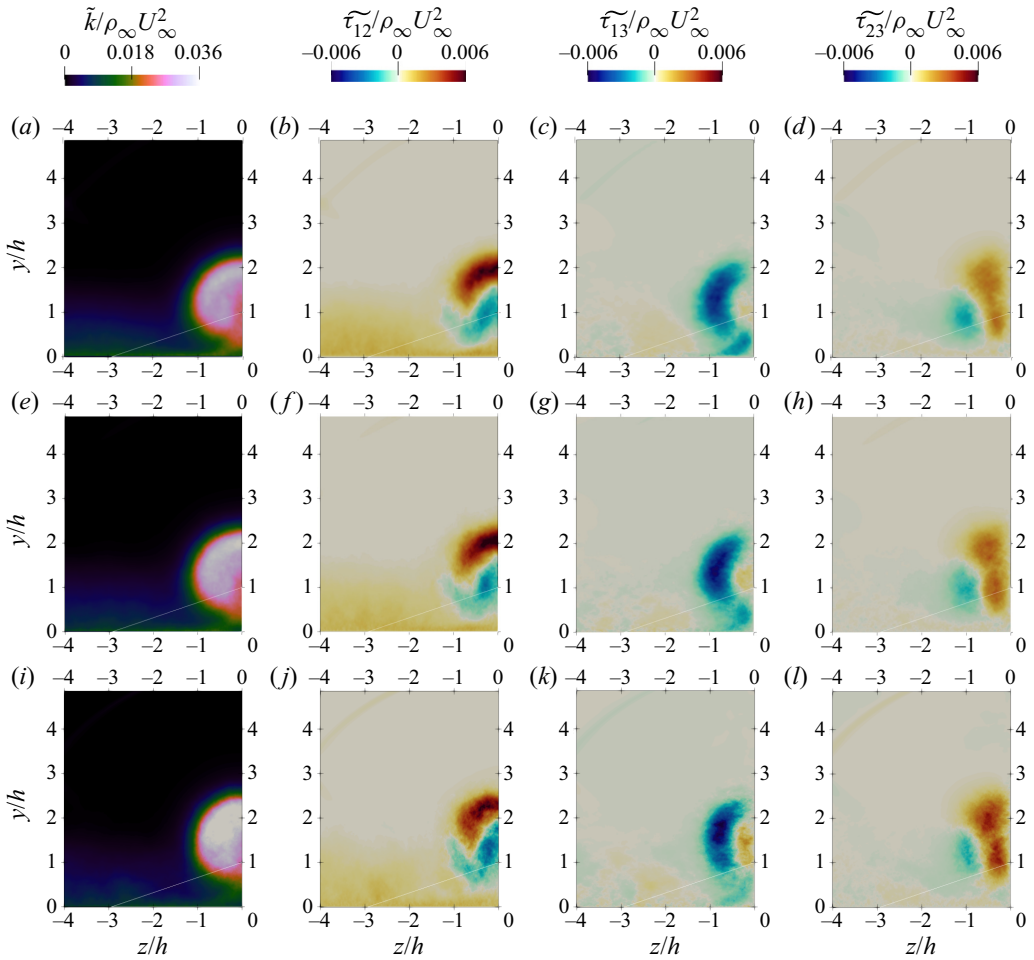
Figure 18. Turbulent kinetic energy $\tilde{k}/\rho_\infty U_\infty^2$ (a,e,i), $\widetilde{\tau_{12}}/\rho_\infty U_\infty^2$ (b,f,j), $\widetilde{\tau_{13}}/\rho_\infty U_\infty^2$ (c,g,k), $\widetilde{\tau_{23}}/\rho_\infty U_\infty^2$ (d,h,l), at $x/h = 8$ for low (a,b,c,d), intermediate (e,f,g,h), high (i,j,k,l) Reynolds number.

In fact, the fluid in the wake is the one captured directly (fluid from the top of the ramp captured by the side vortices) or indirectly (fluid entrained in the near-wall region from outside of the primary vortices) by the MVG flow structures. In both cases, fluid inside the wake was previously close to the wall. However, as a consequence of the imposed adiabatic wall conditions, the aerodynamic heating raises the temperature of this fluid, which thus results in a wake hotter than the corresponding undisturbed flow. The sonic line indicated in white also suggests the thinning of the boundary layer below the wake, due to the energising exchange of momentum promoted by the microramp. Proceeding downstream, the entrainment of colder and faster flow from outside induces an increase in the Mach number, which tends to the undisturbed conditions far from the ramp. In the wake region, even after $15h$ from the trailing edge, we can see that the subsonic region – and the wake in general – is not circular and homogeneous inside. As a matter of fact, the lift-up close to the symmetry plane and the external flow summoning due to the primary vortices makes the magnitude of the Mach number at the centre higher than elsewhere in the wake.

974 A44-22

The principal Reynolds stress components highlight instead that the wake region, with its shear layers and vortical structures, is characterised as expected by an increased turbulent kinetic energy that decays as soon as the wake spreads. Given the larger exposure to the incoming flow, the magnitude of the streamwise velocity fluctuations is more significant in the top part of the wake. At the same time, vertical fluctuations fed by the lift-up of the primary vortex pair decay slowly and are more important at the symmetry plane, where the upwash is maximum. Other regions of intense turbulent activity are noticeable in the field, especially at $x/h = 4$, and represent a trace of the near wake features that rapidly disappears. In particular, initially $\widetilde{\tau_{11}}$ exhibits large values in magnitude also close to the symmetry plane, probably due to the observed volutes, with their secondary KH vortices inside the wake. Moreover, in the lower part at the spanwise centre, strong spanwise fluctuations are highlighted by negative peak values of $\widetilde{\tau_{33}}$, likely caused by the convergence of the primary vortex pair and by the last effects of the bottom secondary vortices.

The Reynolds shear stress $\widetilde{\tau_{12}}$ confirms that the top part of the annular shear layer is related to the most important turbulent mixing, where the maximum value is very close to the experimental measurements of Sun *et al.* (2012) ($-\overline{u'v'}/U_\infty^2 \approx 0.007$, where $(\bullet)'$ indicates fluctuations of a quantity with respect to its Reynolds average). Furthermore, the negative regions in the bottom part of the wake suggest that the bottom shear layer is weaker than the top one, in accordance with the previous observations in § 4.2.4 about the difference in the vertical gradients close and far from the wall.

Figure 18 shows instead a comparison of the Favre-averaged turbulent kinetic energy ($\tilde{k} = -(\widetilde{\tau_{11}} + \widetilde{\tau_{22}} + \widetilde{\tau_{33}})$) and of the transversal shear stress components between the three cases at different Reynolds numbers on an intermediate yz plane at $x/h = 8$. Increasing the Reynolds number does not affect qualitatively the distribution and has more of a quantitative effect on the evolution of the far wake. In particular, the magnitude of the turbulent kinetic energy and of the transversal turbulent stress components in the wake increases with the Reynolds number, indicating an increased mixing especially at the external and internal edges of the wake, where velocity gradients become stronger.

4.4. *Near-wall behaviour*

As we demonstrated throughout the previous discussion, the wake behind a microramp is highly 3-D and, as a result, streamwise and spanwise modulation of the flow behaviour close to the wall is expected. In order to discuss these modifications, we consider in the following the distribution on the wall-parallel plane of the added momentum, introduced by Giepman *et al.* (2014), and of the difference of the friction coefficient between the controlled and uncontrolled cases.

4.4.1. *Added momentum*

To evaluate the efficiency of the momentum transfer towards the near-wall region induced by the presence of the microramp, Giepman *et al.* (2014, 2015, 2016) introduced the so-called added momentum. By including also the density in the definition, the (compressible) added momentum is defined as

$$E = \int_0^{0.43\delta_{99}} \frac{\overline{\rho u^2} - \overline{\rho u^2}_{BL}}{\rho_\infty U_\infty^2} \mathrm{d}y \tag{4.5}$$

where the subscript *BL* indicates the momentum of the uncontrolled boundary layer. An upper limit of integration equal to $0.43\delta_{99}$ is used, since the separation bubble of the
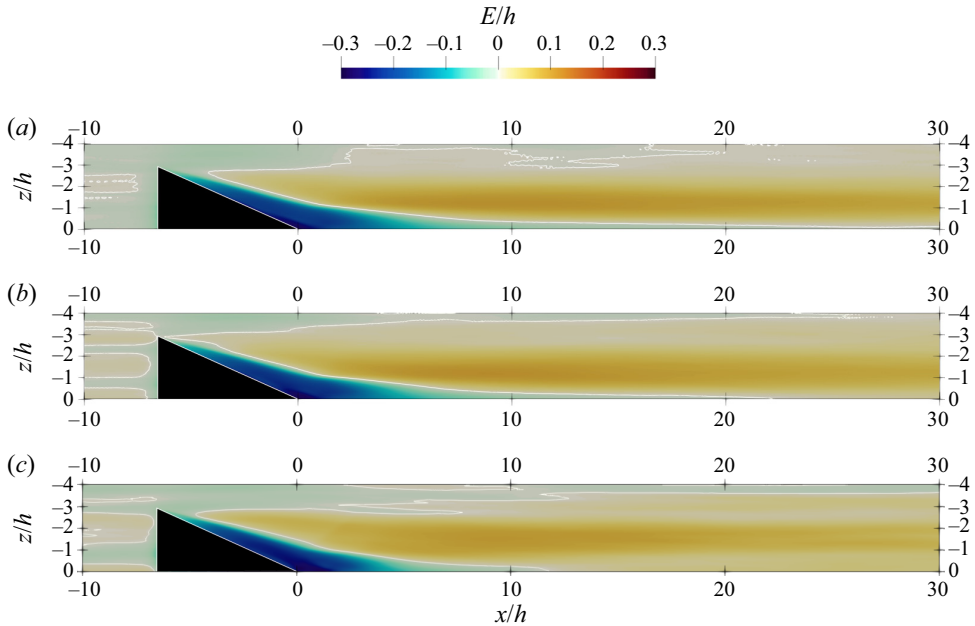
Figure 19. Normalised added momentum in the wall-parallel plane. White lines indicate the points for which $E/h = 0$. Low (*a*), intermediate (*b*) and high (*c*) Reynolds number.

downstream SBLI in the experiments of the cited works was found to be mostly sensitive to the momentum of the lower 43 % boundary layer. Similarly to the other wake features, E is typically scaled by the ramp height.

Contrary to the previous experimental works, which were limited to the symmetry plane only, our numerical database makes it possible to examine the distribution of the added momentum on the entire surface of the bottom wall (figure 19), allowing us to characterise also the spanwise behaviour of the momentum transfer towards the wall.

At the sides of the ramp and close to the symmetry plane, the upward motion induced by the primary and secondary vortices removes momentum from the region close to the wall, thus generating areas with negative E. However, even at the symmetry plane, the added momentum ends up being larger than zero not far from the trailing edge of the ramp (only marginally for the case at low Reynolds). On the other hand, approximately below the primary vortices, a noticeable region of positive E indicates that the helical motion related to the primary vortices brings fresh fluid with high momentum from the sides of the wake towards the plane of symmetry, from higher wall-normal locations to the bottom portion of the domain.

In order to better capture the quantitative differences between the three cases, figure 20 shows the normalised added momentum for the three Reynolds numbers along the spanwise direction at $x/h = 0$, 10 and 30, and along the streamwise direction at $z/h = -b/h$, $-0.5b/h$ and 0. Although the results agree well with the experimental results of Giepman *et al.* (2016) at the symmetry plane, confirming the trend for increasing Reynolds number, the plots highlight again that the only added momentum at the spanwise centre is insufficient to portray appropriately the overall transfer to the wall induced by the microramp wake. In fact, we can see that in the far wake, E/h is limited at the symmetry plane but, at the same time, is high below the cores of the primary vortex pair, where the most important addition of momentum takes place. Concerning the differences between the cases, a clear trend for increasing Reynolds number is not easily recognisable.
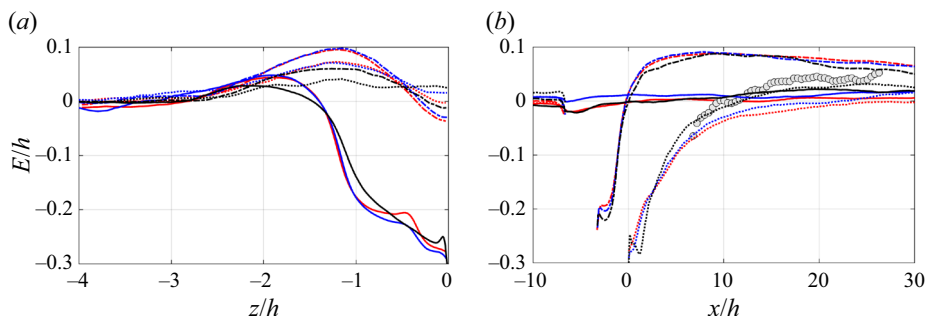
974 A44-24

Figure 20. Normalised added momentum distribution (*a*) along the spanwise direction at $x/h = 0$ (solid lines), 10 (dash-dotted lines), 30 (dotted lines); (*b*) along the streamwise direction at $z/h = -b/h$ (solid lines), $-0.5b/h$ (dash-dotted lines), 0 (dotted lines), with b being the half of the spanwise extent of the microramp. Circles denote experiments by Giepman *et al.* (2016) at $M_\infty = 2.0$ and $Re_\theta = 6.7 \times 10^4$: (red lines) $Re_\tau = 500$; (blue lines) $Re_\tau = 1000$; (black lines) $Re_\tau = 2000$.

We showed in the previous sections that increasing the Reynolds number means dealing with stronger vortical structures, which lift up the wake faster and move – reasonably – more fluid. As a consequence, the region with negative added momentum at the spanwise centre shrinks progressively as the Reynolds number is increased. However, contrary to what was expected, the peak added momentum at high Reynolds number is smaller than the other cases. This result could be related to the fact that if the low-momentum region rises faster because of the increased upwash, the azimuthal motion of the primary vortices affects only fluid that is farther from the wall, and so, despite the circulation being larger, the resulting added momentum is smaller. Moreover, since for different Reynolds numbers, the primary vortices have different trajectories (vortices close to the sidewalls of the ramp and more abrupt alignment to the streamwise direction for larger Reynolds numbers) and the wakes have different streamwise evolutions, comparing the added momentum for the three conditions at fixed x/h and z/h can be misleading. For these reasons, further analysis in future work is needed to better understand the balance and scaling of the different contrasting aspects.

4.4.2. *Relative friction coefficient*

Figure 21 reports the percentage relative difference of the Favre-averaged skin friction coefficient at the wall of the flat plate ($C_f = 2\tilde{\tau}_w/\rho_\infty U_\infty^2$) between the controlled and the uncontrolled cases ($\Delta C_f = C_f - C_{f,BL}$). In particular, since the spanwise friction component $\tilde{\tau}_z = (\partial \tilde{w}/\partial y)_w$ was far smaller in magnitude than the streamwise component $\tilde{\tau}_x = (\partial \tilde{u}/\partial y)_w$, we consider in the following the approximation for the controlled case that $\tilde{\tau}_w \approx \tilde{\tau}_x$. In the C_f contours, we find many flow features also observed in the wake analysis, confirming the insights from the added momentum. The primary and secondary vortices at the sides of the ramp are highlighted by regions of enhanced and reduced friction, whereas the trailing edge shock is visible in the transversal low-friction region right after the trailing edge of the ramp. After the near wake, the entrainment of high-momentum fluid induced by the primary vortices is responsible for a prolonged region of higher friction, which persists even $30h$ downstream of the microramp. The contours point out the significant streamwise and spanwise variation of the boundary layer properties, which plays a major role in the SBLI control mechanism. In this regard, Babinsky *et al.* (2009) showed that an important effect of microramp arrays upstream of the interaction region in two-dimensional SBLIs consists in the modulation of the separated flow area, which is broken up in multiple individual pockets of 3-D reverse flow, separated by regions of attached flow.
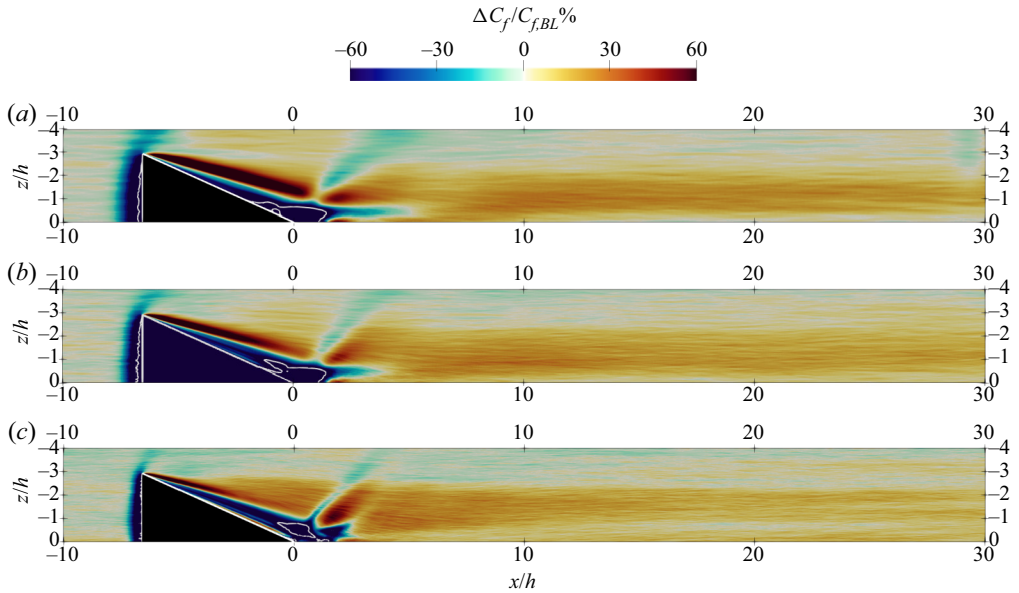
$$\Delta C_f / C_{f,BL}\%$$

Figure 21. Percentage difference of the skin friction coefficient between the controlled and uncontrolled boundary layer. White lines indicate the points for which $(\partial\tilde{u}/\partial y)_w = 0$. Low (*a*), intermediate (*b*) and high (*c*) Reynolds number.

Finally, since the wake rises faster at higher Reynolds number, we note that increasing Re_τ the relative skin friction increase becomes weaker in the far wake.

5. Conclusions

Microramp MVGs are promising devices proposed to passively control flow separation and mitigate SBLI adverse effects. This work presents a campaign of DNSs which aims at examining the effects of a microramp immersed in a supersonic turbulent boundary layer for different Reynolds numbers, approaching the values achieved in experiments. Three conditions are considered, with friction Reynolds number Re_τ equal to 500, 1000 and 2000, fixed free stream Mach number M_∞ equal to 2, and fixed shape and relative height of the ramp with respect to the uncontrolled boundary layer thickness ($h/\delta_{99} = 2/3$).

The high fidelity of the DNS database and the opportunity to access completely the flow field make it possible to observe in detail the instantaneous organisation of the turbulent structures, disclosing the formation of primary, secondary, and almost-toroidal vortices in the wake, but also of the system of shock waves interacting with the wake, hardly addressed in the literature. We observe in particular two shocks nearly conical in shape, which originate at the foot and trailing edge of the microramp and leave a visible signature on the flow close to the wall, as revealed by the distributions of the skin friction coefficient and of the added momentum. Moreover, high-fidelity simulations like those in this paper offer comprehensive and reliable data that are essential to improve the accuracy and the physical representation of lower-fidelity or reduced-order models, which are still the only viable way to explore larger spaces of parameters for design purposes.

In order to describe the evolution of the boundary layer and that of the wake, and to assess the control efficiency of the device, we take into consideration the streamwise

974 A44-26

development of the streamwise and wall-normal velocity components at the symmetry plane. We find important Reynolds number effects in the range considered, although the highest Reynolds number case shows good agreement with recent experiments at $Re_\tau \approx 5000$, confirming the relevance of our high-Reynolds number data set.

To complete the picture of the wake development, we then assess the self-similarity of the velocity profiles in the far wake, following the work of Sun *et al.* (2020). The results show that self-similarity is not strictly recovered close to the wall, where the bottom secondary vortices have a prolonged influence on the streamwise velocity. Similarly, self-similarity breaks down in the outer part of the wake, where shock waves leave their imprint.

The 3-D distribution of the Favre-averaged flow statistics highlights then the presence of a complex organisation of the vortical structures inside the low-momentum region, especially in the near field. On the basis of the mean vorticity components, we propose a model of the internal structure of the primary vortices close to the trailing edge, which is fundamental for the understanding of the following development in the far field. According to the model, primary vortices are initially convoluted at the sides of the ramp and join naturally the KH vortices that take place on top of the wake. The model is also able to explain the experimental observations of internal KH vortices inside the wake in wall-parallel planes in Sun *et al.* (2012), and adds further details to the understanding of the almost-toroidal vortices around the low-momentum area.

We also analyse the Reynolds stress components, which indicate regions of intense turbulent activity and highlight the annular shear layer around the wake. The distribution of the Reynolds stresses also confirms that the legs of the external KH vortices do not close at the bottom, but rather join the motion induced by the primary vortices inside the wake. Moreover, results show that the structure of the turbulence in the far wake of a microramp is fundamentally different from that of an undisturbed boundary layer but is rather characterised by significant anisotropy, as shown by Mole *et al.* (2022). Thus, further study will be necessary to assess the potential consequences of these changes if a SBLI were located downstream.

Finally, we focus on the changes in the boundary layer close to the wall, which allows us to assess the spanwise flow modulation induced by the microramp. The added momentum, introduced by Giepman *et al.* (2014), and the relative difference in skin friction coefficient between the controlled and uncontrolled cases, confirm the control mechanism of the microramp, which induces two counter-rotating vortices bringing high-momentum fluid closer to the wall thus increasing the local skin friction coefficient.

Moreover, results allow us to advance a prediction about the control effectiveness of microramps. Even though vortical structures are those steering momentum transfer, shape factors show no sign of recovery in the mean boundary layer properties even after $x/h = 30$, where the intensity of the vortices is low. This observation suggests that the effectiveness in controlling SBLI could be rather insensitive to the position of the microramp, for large relative distances. Hence, we expect good control performance in a fairly wide range of shock positions. Simulations in the presence of SBLI are currently ongoing to verify this conjecture.

As anticipated above, almost all the quantities considered in this study reveal a non-negligible dependence on the Reynolds number. To sum up, according to the results obtained, the main effects due to low Reynolds number observed are as follows.

(i) Turbulent structures have a less coherent roll-up around the wake deficit, leading to weaker almost-toroidal vortices.

(ii) Wake features do not scale with the geometric size of the ramp and thus depend also on the incoming flow properties. If one uses the height *h* to scale typical wake features, results indicate a slower and weaker development of the wake for lower Reynolds numbers.

(iii) The self-similarity of the wake, especially in its top portion, is less strict.

(iv) Smaller momentum captured by the microramp at lower Reynolds number means smaller circulation of the side vortices, which leads to a reduction of the induced upwash and thus a decrease in the lift-up of the wake.

(v) Side vortices become parallel more gradually. At higher Reynolds number, the primary vortices remain close to the sidewalls of the ramp longer, the separation near the trailing edge of the ramp starts more downstream and is slightly more prolonged in the streamwise direction.

(vi) Weaker vortices at low Reynolds number, with a slower wake development, lead also to a slower transfer of momentum towards the wall, which is visible in the smaller added momentum especially at the symmetry plane. At the same time, weaker vortices means slower lift-up, which in the end prolongs the region for which the wake is sufficiently close to the wall to influence the increase in momentum transfer and in skin friction behind the ramp.

Author ORCIDs.

ⓘ G. Della Posta https://orcid.org/0000-0001-5516-9338;

ⓘ M. Blandino https://orcid.org/0009-0008-3478-1446;

ⓘ D. Modesti https://orcid.org/0000-0003-2214-5799;

ⓘ F. Salvadore https://orcid.org/0000-0002-1829-3388;

ⓘ M. Bernardini https://orcid.org/0000-0001-5975-3734.

REFERENCES

ANDERSON, B., TINAPPLE, J. & SURBER, L. 2006 Optimal control of shock wave turbulent boundary layer interactions using micro-array actuation. *AIAA Paper* 2006-3197.

ASHILL, P.R., FULKER, J.L. & HACKETT, K.C. 2005 A review of recent developments in flow control. *Aeronaut. J.* **109** (1095), 205–232.

BABINSKY, H., LI, Y. & FORD, C.W.P. 2009 Microramp control of supersonic oblique shock-wave/boundary-layer interactions. *AIAA J.* **47** (3), 668–675.

BABINSKY, H. & OGAWA, H. 2008 SBLI control for wings and inlets. *Shock Waves* **18** (2), 89–96.

BATCHELOR, G.K. 1964 Axial flow in trailing line vortices. *J. Fluid Mech.* **20** (4), 645–658.

BERNARDINI, M., DELLA POSTA, G., SALVADORE, F. & MARTELLI, E. 2023*a* Unsteadiness characterisation of shock wave/turbulent boundary-layer interaction at moderate Reynolds number. *J. Fluid Mech.* **954**, A43.

BERNARDINI, M., MODESTI, D., SALVADORE, F. & PIROZZOLI, S. 2021 STREAmS: a high-fidelity accelerated solver for direct numerical simulation of compressible turbulent flows. *Comput. Phys. Commun.* **263**, 107906.

BERNARDINI, M., MODESTI, D., SALVADORE, F., SATHYANARAYANA, S., DELLA POSTA, G. & PIROZZOLI, S. 2023*b* STREAmS-2.0: supersonic turbulent accelerated Navier–Stokes solver version 2.0. *Comput. Phys. Commun.* **285**, 108644.

BLINDE, P.L., HUMBLE, R.A., VAN OUDHEUSDEN, B.W. & SCARANO, F. 2009 Effects of micro-ramps on a shock wave/turbulent boundary layer interaction. *Shock Waves* **19** (6), 507–520.

BO, W., WEIDONG, L., YUXIN, Z., XIAOQIANG, F. & CHAO, W. 2012 Experimental investigation of the micro-ramp based shock wave and turbulent boundary layer interaction control. *Phys. Fluids* **24** (5), 055110.

CLEMENS, N.T. & NARAYANASWAMY, V. 2014 Low-frequency unsteadiness of shock wave/turbulent boundary layer interactions. *Annu. Rev. Fluid Mech.* **46** (1), 469–492.

DAVIS, R.W. & MITCHELL, G.A. 1968 Performance of centerbody vortex generators in an axisymmetric mixed-compression inlet at Mach numbers from 2.0 to 3.0. *Tech. Rep.* TN D-4675. NASA.

DOLLING, D.S. 2001 Fifty years of shock-wave/boundary-layer interaction research: what next? *AIAA J.* **39** (8), 1517–1531.

GAITONDE, D.V. 2015 Progress in shock wave/boundary layer interactions. *Prog. Aerosp. Sci.* **72**, 80–99.

GHOSH, S., CHOI, J. & EDWARDS, J.R. 2010 Numerical simulations of effects of micro vortex generators using immersed-boundary methods. *AIAA J.* **48** (1), 92–103.

GIEPMAN, R.H.M., SCHRIJER, F.F.J. & VAN OUDHEUSDEN, B.W. 2014 Flow control of an oblique shock wave reflection with micro-ramp vortex generators: effects of location and size. *Phys. Fluids* **26** (6), 066101.

GIEPMAN, R., SRIVASTAVA, A., SCHRIJER, F.F.J. & VAN OUDHEUSDEN, B.W. 2015 The effects of Mach and Reynolds number on the flow mixing properties of micro-ramp vortex generators in a supersonic boundary layer. *AIAA Paper* 2015-2779.

GIEPMAN, R.H.M., SRIVASTAVA, A., SCHRIJER, F.F.J. & VAN OUDHEUSDEN, B.W. 2016 Mach and Reynolds number effects on the wake properties of microramps. *AIAA J.* **54** (11), 3481–3494.

GRÉBERT, A., BODART, J., JAMME, S. & JOLY, L. 2018 Simulations of shock wave/turbulent boundary layer interaction with upstream micro vortex generators. *Intl J. Heat Fluid Flow* **72**, 73–85.

HERRMANN, C. & KOSCHEL, W. 2002 Experimental investigation of the internal compression inside a hypersonic intake. *AIAA Paper* 2002-4130.

JIANG, G.S. & SHU, C.W. 1996 Efficient implementation of weighted ENO schemes. *J. Comput. Phys.* **126** (1), 202–228.

LEE, S. & LOTH, E. 2009 Supersonic boundary-layer interactions with various micro-vortex generator geometries. *Aeronaut. J.* **113** (1149), 683–697.

LEE, S., LOTH, E., GEORGIADIS, N.J. & DEBONIS, J.R. 2011 Effect of Mach number on flow past microramps. *AIAA J.* **49** (1), 97–110.

LI, Q. & LIU, C. 2010 Declining angle effects of the trailing edge of a microramp vortex generator. *J. Aircraft* **47** (6), 2086–2095.

LI, Q. & LIU, C. 2011 Implicit LES for supersonic microramp vortex generator: new discoveries and new mechanisms. *Model. Simul. Engng* **2011**, 934982.

LIN, J.C. 2002 Review of research on low-profile vortex generators to control boundary-layer separation. *Prog. Aerosp. Sci.* **38** (4), 389–420.

LOTH, E. 2000 Smart mesoflaps for control of shock boundary layer interactions. *AIAA Paper* 2000-2476.

LU, F.K., LI, Q. & LIU, C. 2012 Microvortex generators in high-speed flow. *Prog. Aerosp. Sci.* **53**, 30–45.

LU, F.K., PIERCE, A., SHIH, Y., LIU, C. & LI, Q. 2010 Experimental and numerical study of flow topology past micro-vortex generators. *AIAA Paper* 2010-4463.

LUND, T.S., WU, X. & SQUIRES, K.D. 1998 Generation of turbulent inflow data for spatially-developing boundary layer simulations. *J. Comput. Phys.* **140** (2), 233–258.

MCCORMICK, D.C. 1993 Shock/boundary-layer interaction control with vortex generators and passive cavity. *AIAA J.* **31** (1), 91–96.

MODESTI, D., SATHYANARAYANA, S., SALVADORE, F. & BERNARDINI, M. 2022 Direct numerical simulation of supersonic turbulent flows over rough surfaces. *J. Fluid Mech.* **942**, A44.

MOLE, A., SKILLEN, A. & REVELL, A. 2022 The interaction of longitudinal vortex pairs with a turbulent boundary layer. *J. Fluid Mech.* **953**, A31.

PANARAS, A.G. & LU, F.K. 2015 Micro-vortex generators for shock wave/boundary layer interactions. *Prog. Aerosp. Sci.* **74**, 16–47.

PIQUET, A., ROUSSEL, O. & HADJADJ, A. 2016 A comparative study of Brinkman penalization and direct-forcing immersed boundary methods for compressible viscous flows. *Comput. Fluids* **136**, 272–284.

PIROZZOLI, S. 2010 Generalized conservative approximations of split convective derivative operators. *J. Comput. Phys.* **229** (19), 7180–7190.

PITT FORD, C. & BABINSKY, H. 2007 Micro-ramp control for oblique shock wave/boundary layer interactions. *AIAA Paper* 2007-4115.

POINSOT, T.J. & LELE, S.K. 1992 Boundary conditions for direct simulations of compressible viscous flows. *J. Comput. Phys.* **101** (1), 104–129.

SALVADORE, F., MEMMOLO, A., MODESTI, D., DELLA POSTA, G. & BERNARDINI, M. 2022 Direct numerical simulation of a micro-ramp in a high-Reynolds number supersonic turbulent boundary layer. In *75th APS/DFD, Gallery of Fluid Motion*. American Physical Society. https://www.youtube.com/watch?v=o8olmjiWSl8.

SATHYANARAYANA, S., BERNARDINI, M., MODESTI, D., PIROZZOLI, S. & SALVADORE, F. 2023 High-speed turbulent flows towards the exascale: STREAmS-2 porting and performance. arXiv:2304.05494.

SILLERO, J.A., JIMÉNEZ, J. & MOSER, R.D. 2013 One-point statistics for turbulent wall-bounded flows at Reynolds numbers up to $\delta^+ \simeq 2000$. *Phys. Fluids* **25** (10), 105102.

SPALART, P.R., MOSER, R.D. & ROGERS, M.M. 1991 Spectral methods for the Navier–Stokes equations with one infinite and two periodic directions. *J. Comput. Phys.* **96** (2), 297–324.

SUN, D., CHEN, J., LI, C., LIU, P., GUO, Q. & YUAN, X. 2020 On the wake structure of a micro-ramp vortex generator in hypersonic flow. *Phys. Fluids* **32** (12), 126111.

SUN, Z., SCARANO, F., VAN OUDHEUSDEN, B.W., SCHRIJER, F.F.J., WANG, X., YAN, Y. & LIU, C. 2013 Numerical and experimental investigations of the flow behind a supersonic micro-ramp. *AIAA Paper* 2013-0954.

SUN, Z., SCARANO, F., VAN OUDHEUSDEN, B.W., SCHRIJER, F.F.J., YAN, Y. & LIU, C. 2014*a* Numerical and experimental investigations of the supersonic microramp wake. *AIAA J.* **52** (7), 1518–1527.

SUN, Z., SCHRIJER, F.F.J., SCARANO, F. & VAN OUDHEUSDEN, B.W. 2012 The three-dimensional flow organization past a micro-ramp in a supersonic boundary layer. *Phys. Fluids* **24** (5), 055105.

SUN, Z., SCHRIJER, F.F.J., SCARANO, F. & VAN OUDHEUSDEN, B.W. 2014*b* Decay of the supersonic turbulent wakes from micro-ramps. *Phys. Fluids* **26** (2), 025115.

TAMBE, S., SCHRIJER, F.F.J & VAN OUDHEUSDEN, B.W. 2021 Relation between geometry and wake characteristics of a supersonic microramp. *AIAA J.* **59** (11), 4501–4513.

WHEELER, G.O. 1984 Means for maintaining attached flow of a flowing medium. US Patent 4,455,045.

ZHOU, J., ADRIAN, R.J., BALACHANDAR, S. & KENDALL, T.M. 1999 Mechanisms for generating coherent packets of hairpin vortices in channel flow. *J. Fluid Mech.* **387**, 353–396.